

Exhaustive probabilistic neural network for attribute selection and supervised seismic facies classification

David Lubo-Robles¹, Thang Ha¹, Sivaramakrishnan Lakshminarayanan², Kurt J. Marfurt¹, and Matthew J. Pranter¹

Abstract

Machine learning (ML) algorithms, such as principal component analysis, independent component analysis, self-organizing maps, and artificial neural networks, have been used by geoscientists to not only accelerate the interpretation of their data, but also to provide a more quantitative estimate of the likelihood that any voxel belongs to a given facies. Identifying the best combination of attributes needed to perform either supervised or unsupervised ML tasks continues to be the most-asked question by interpreters. In the past decades, stepwise regression and genetic algorithms have been used together with supervised learning algorithms to select the best number and combination of attributes. For reasons of computational efficiency, these techniques do not test all of the seismic attribute combinations, potentially leading to a suboptimal classification. In this study, we have developed an exhaustive probabilistic neural network (PNN) algorithm that exploits the PNN's capacity in exploring nonlinear relationships to obtain the optimal attribute subset that best differentiates target seismic facies of interest. We determine the efficacy of our proposed workflow in differentiating salt from nonsalt seismic facies in a Eugene Island seismic survey, offshore Louisiana. We find that from seven input candidate attributes, the exhaustive PNN is capable of removing irrelevant attributes by selecting a smaller subset of four seismic attributes. The enhanced classification using fewer attributes also reduces the computational cost. We then use the resulting facies probability volumes to construct the 3D distribution of the salt diapir geobodies embedded in a stratigraphic matrix.

Introduction

The past two decades have seen the increasing use of unsupervised and supervised machine-learning (ML) techniques for geophysical applications such as fault detection (Di et al., 2017, 2019; Wu et al., 2019), seismic facies analysis (Roy et al., 2014; Zhao et al., 2015; Amin et al., 2017; Long et al., 2018; Wrona et al., 2018), and prediction of well-log properties based on seismic attributes (Hampson et al., 2001; Dorrington and Link, 2004). For seismic facies classification, interpreters select a suite of seismic attributes as input to define a multivariate classification task. Common attributes used for classification include the same geometric, instantaneous, spectral, textural, and geomechanical attributes that human interpreters have found to be useful.

In supervised learning, the goal is to differentiate one or more interpreter-defined target seismic facies from each other and from an undifferentiated background. In unsupervised learning, the goal is to provide a rela-

tively unbiased classification of the dominant facies which may or may not have geologic significance. However, whether the interpreter is performing an unsupervised or supervised seismic facies classification, the choice of attributes and the selection of training data strongly bias the results. Moreover, selecting the best attribute combination to distinguish different target facies requires significant understanding of not only geologic processes and the seismic expression of structural and stratigraphic patterns, but also of the features measured by seismic attributes.

There are three other challenges in using ML for seismic facies analysis: (1) the Hughes (1968) phenomenon in which the classification performance of a ML algorithm decreases after reaching a certain number of input features, (2) the overwhelming number of attributes that limit the interpreter's ability to interact with all of the information available (Roden et al., 2015), and (3) the presence of redundant and irrelevant attributes that do not provide any additional information and

¹The University of Oklahoma, School of Geosciences, Norman, Oklahoma 73019, USA. E-mail: davidlubo@ou.edu (corresponding author); Thang.N.Ha-1@ou.edu; kmarfurt@ou.edu; matthew.pranter@ou.edu.

²The University of Oklahoma, School of Computer Science, Norman, Oklahoma 73019, USA. E-mail: varahan@ou.edu.

Manuscript received by the Editor 11 May 2020; revised manuscript received 22 September 2020; published ahead of production 24 December 2020; published online 07 April 2021. This paper appears in *Interpretation*, Vol. 9, No. 2 (May 2021); p. T421–T441, 19 FIGS., 1 TABLE. <http://dx.doi.org/10.1190/INT-2020-0102.1>. © 2021 Society of Exploration Geophysicists and American Association of Petroleum Geologists

create confusion for human interpreters (Barnes, 2007) and, at best, increased cost for ML algorithms.

A partial solution is dimensionality reduction. Principal component analysis (PCA) and independent component analysis are simple projection techniques that find the statistically most important features (Guo et al., 2009; Qi and Castagna, 2013; Chopra and Marfurt, 2014; Honorio et al., 2014; Roden et al., 2015; Lubo-Robles and Marfurt, 2019). Generative topographic maps (GTM) and self-organizing maps are unsupervised learning algorithms in which a multidimensional data set is projected into a lower dimensional space to extract the most valuable information from the data (Roy et al., 2014; Roden et al., 2015; Zhao et al., 2015; Qi et al., 2016; Zhao et al., 2018). If one allows a large number of classes (colors), the classification is approximately continuous, with the final “categorical” classification defining specific seismic facies provided by the human interpreter. Once the major facies have been mapped and their attribute sensitivity are quantified, a smaller suite of attributes or linear combinations of attributes can be used for supervised learning.

Considerably more progress has been made in predicting continuous variables from seismic attribute data. Working with seismic attributes and well-log data, Hampson et al. (2001) use stepwise multilinear regression to choose the best number and collection of seismic attributes to predict a desired well-log property. Dorrington and Link (2004) generalize this approach by using a genetic algorithm together with a multilayer feedforward network to select seismic attributes for porosity prediction. Support vector machine (SVM) algorithms define weights to be applied to the different attributes to achieve the desired separation between seismic facies. In their work, Chang-kai and Wen-kai (2010) use those attributes with larger SVM weights to construct a smaller subset of attributes to differentiate reservoir from nonreservoir seismic facies. Amin et al. (2017) use information theory to rank the seismic attributes and determine the optimal attribute subset for salt-dome detection.

Wang et al. (2015) combine a rough sets algorithm with PCA to reduce the number of attributes used as input for porosity prediction. Finally, Galvis et al. (2017) first use a relevancy filter to discard attributes showing high correlation and then apply a wrapper forward method selection based on k -means to select the optimal combination of attributes to identify surface waves in multicomponent common-shot gathers.

One key limitation to these workflows is that they do not test all the possible combinations of input features; thus, they can miss important relationships existing between the attributes. Recently, Qi et al. (2020) evaluate all possible combinations of seismic attributes to differentiate among salt, mass-transport deposits (MTDs), and conformal sediments using a semisupervised learning technique consisting of applying Gaussian mixture models (GMMs) and the Bhattacharyya distance to measure the similarity between two GMMs per facies

and select the optimal combination associated with the maximum average cumulative distance, and then GTM is applied to perform an unsupervised seismic facies classification.

In this study, we propose to perform an exhaustive search in which all possible $2^M - 1$ combinations are tested, where M represents the number of input seismic attributes. Because testing all possible combinations of attributes is computationally expensive and the algorithm's complexity is proportional to the number of input attributes, we use a supervised ML technique called the probabilistic neural network (PNN), which is based on well-established Gaussian statistics and allows for a more robust probability density function (PDF) estimation based on Parzen windows and Bayes's criteria to provide simple, fast, and repeatable training in which only the smoothing parameter r requires optimization.

By coupling an exhaustive search algorithm with the PNN, we can explore nonlinear relationships between seismic attributes and seismic facies. The goal of our “exhaustive PNN” is to test all possible combinations of seismic attributes, reject irrelevant and redundant attributes, provide the optimal combination to distinguish salt from siliciclastic seismic facies, and perform a supervised seismic facies classification.

We begin our paper with a summary of the mechanics of PNN applied to seismic facies classification. We then describe our exhaustive search algorithm to create different subsets of seismic attributes that are then provided to a PNN to measure their performance. After selection of the best combination, we apply a first-order gradient optimization technique called Adam to further improve the performance of the neural network.

Next, we apply our algorithm to the Eugene Island 3D seismic survey located in the Gulf of Mexico. To differentiate the low-amplitude, discontinuous reflectors associated with salt diapirs from the high-amplitude, parallel reflectors associated with the surrounding conformal sedimentary layers, we use discontinuity, texture, and nonparallelism attributes. We also manually define the target facies of the training and validation data sets to represent salt diapirs and conformal reflectors. Given the optimal combination of seismic attributes, we perform a supervised seismic facies classification and analyze whether the proposed workflow can determine the best combination of seismic attributes for the desired classification task. An appendix provides mathematical details explaining how the algorithm works.

Geologic background

The Eugene Island minibasin is a giant Plio-Pleistocene oil and gas field located offshore Louisiana in the outer continental shelf of the Gulf of Mexico (Alexander and Flemings, 1995; Joshi and Appold, 2016). Following Alexander and Flemings (1995), the Eugene Island minibasin evolution can be described in three phases.

The first phase of the evolution is characterized by the deposition of distal deltaic sands, bathyal and pro-

delta shales, and turbidites on top of a salt sheet. This sediment loading caused the salt sheet to migrate outward laterally, creating a new accommodation space in the area (Alexander and Flemings, 1995; Joshi and Appold, 2016). The second phase is related to high sediment accumulation rates due to salt withdrawal and is characterized by lowstand deltas associated with deposition of mud and sand sequences (Alexander and Flemings, 1995; Joshi and Appold, 2016). Finally, the third phase is associated with fluvial deposits and a decrease of salt withdrawal in which little accommodation space was further developed (Alexander and Flemings, 1995; Joshi and Appold, 2016).

Data set

The Eugene Island seismic survey is located in the Gulf of Mexico, offshore Louisiana, and it has an area of approximately 306 km². For this study, the seismic volume consists of 700 inlines and 700 crosslines with a bin size of 82.5 × 82.5 ft and a record length of 3 s.

Figure 1a shows a representative vertical slice along inline 521 through the seismic amplitude volume. We observe a salt diapir (salt diapir 1; the red arrow) associated with salt withdrawal during the prodelta and proximal deltaic phases of deposition (Alexander and Flemings, 1995; Joshi and Appold, 2016) surrounded by high-amplitude, laterally continuous conformal reflectors. In general, salt diapir 1 is characterized by low-amplitude, discontinuous reflectors. However, crossing coherent migration artifacts (the blue arrow) associated with the high P-wave velocity and geometry of the salt (Jones and Davison, 2014) is seen inside salt diapir 1.

Also, we show a time slice at $t = 2$ s through the seismic amplitudes in the Eugene Island survey (Figure 1b). Besides salt diapir 1, we observe the presence of another salt diapir (salt diapir 2) that is also characterized by low-amplitude, discontinuous reflectors.

Methods

PNN

The PNN is a type of feedforward neural network widely used in classification tasks. To classify a given voxel, the PNN uses Parzen windows and Bayes's criteria to estimate its PDF and assigns it to the class in which the PDF is largest (Specht, 1990; Masters, 1995; Hajmeer and Basheer, 2002). Several kernels can be used during the Parzen window estimation; however, the most common kernel used is the Gaussian function due to its high performance and simple computation (Masters, 1995). We begin by subdividing our volume into three parts: (1) labeled training data used to define several of the necessary parameters for the model, (2) labeled validation data used to test our algorithm's performance during the learning phase, and

(3) the remainder of the volume representing test/unseen data to be classified by the trained PNN. In our application, the training and validation data are generated by the human interpreter drawing polygons around facies of interest. In addition, another approach to assess the effectiveness of the model when classifying previously unseen data can be defining a test data set by picking polygons for the seismic facies of interest but using salt diapir 2 and its surrounding conformal sediments instead of performing the seismic facies classification in the whole volume. The m th attribute at a training sample n , a_{nm} , defines a component of a seismic attribute vector \mathbf{a}_n . Given our training data composed of a set of training seismic attributes vectors \mathbf{a} , the average estimated PDF $g_k(\mathbf{x})$ is given by

$$g_k(\mathbf{x}) = \frac{1}{N_k} \sum_{n=1}^{N_k} \exp \left[-\sum_{m=1}^M \frac{(x_m - a_{nm})^2}{r^2} \right], \quad (1)$$

where N_k is the number of training samples associated with the k th class defined by the training data, M is the number of input attributes, \mathbf{x} is a validation seismic attribute vector, and r is a smoothing parameter that requires careful selection through training.

The PNN architecture consists of four layers (1) the input layer, (2) the pattern layer, (3) the summation layer, and (4) the output layer (Specht, 1990; Masters, 1995) (Figure 2a). In the input layer, an unknown input sample is selected to be classified into a particular class. Second, in the pattern layer, the PNN starts by computing the difference between the validation and the training attributes (Figure 2b). This difference is then input into the Gaussian activation function in equation 1 (Masters, 1995). In the summation layer, the PNN calculates the average estimated density function $g_k(\mathbf{x})$ for each class. Finally, in the output layer (Figure 2b), the PNN assigns the unknown sample to class q where

$$g_q(\mathbf{x}) \geq g_k(\mathbf{x}) \quad k = 1, 2, \dots, K. \quad (2)$$

PNN also provides confidence estimates of the classification (Masters, 1995) given by

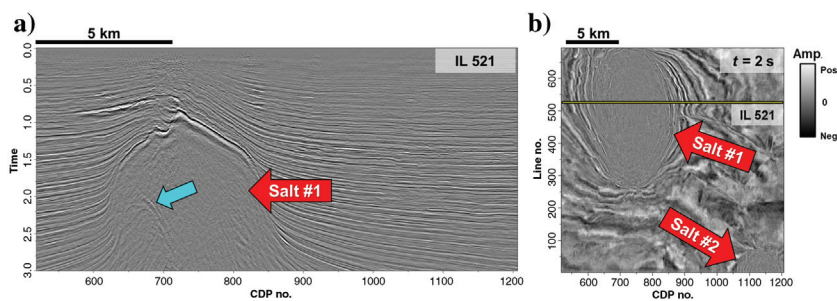


Figure 1. Eugene Island seismic survey. (a) Vertical slice along inline 521. Salt diapir 1 is characterized by low-amplitude, discontinuous reflectors. Crossing coherent migration artifacts (the blue arrow) are also visible inside salt diapir 1. (b) Representative time slice at $t = 2$ s. Another salt diapir (salt diapir 2) also characterized by low-amplitude, discontinuous reflectors is visible in the seismic survey.

$$P_k(\mathbf{x}) = \frac{\frac{1}{N_k} \sum_{n=1}^{N_k} \delta_{nk} \exp \left[-\sum_{m=1}^M \frac{(x_m - a_{nm})^2}{r^2} \right]}{\sum_{k=1}^K \left[\frac{1}{N_k} \sum_{n=1}^{N_k} \delta_{nk} \exp \left[-\sum_{m=1}^M \frac{(x_m - a_{nm})^2}{r^2} \right] \right]}, \quad (3)$$

where P_k represents the normalized probabilities given by the estimated PDF of each class k , $g_k(\mathbf{x})$, divided by the sum of all of the density functions of all K classes. The Kronecker delta δ_{nk} is equal to one if the training case n belongs to class k , and it is zero otherwise.

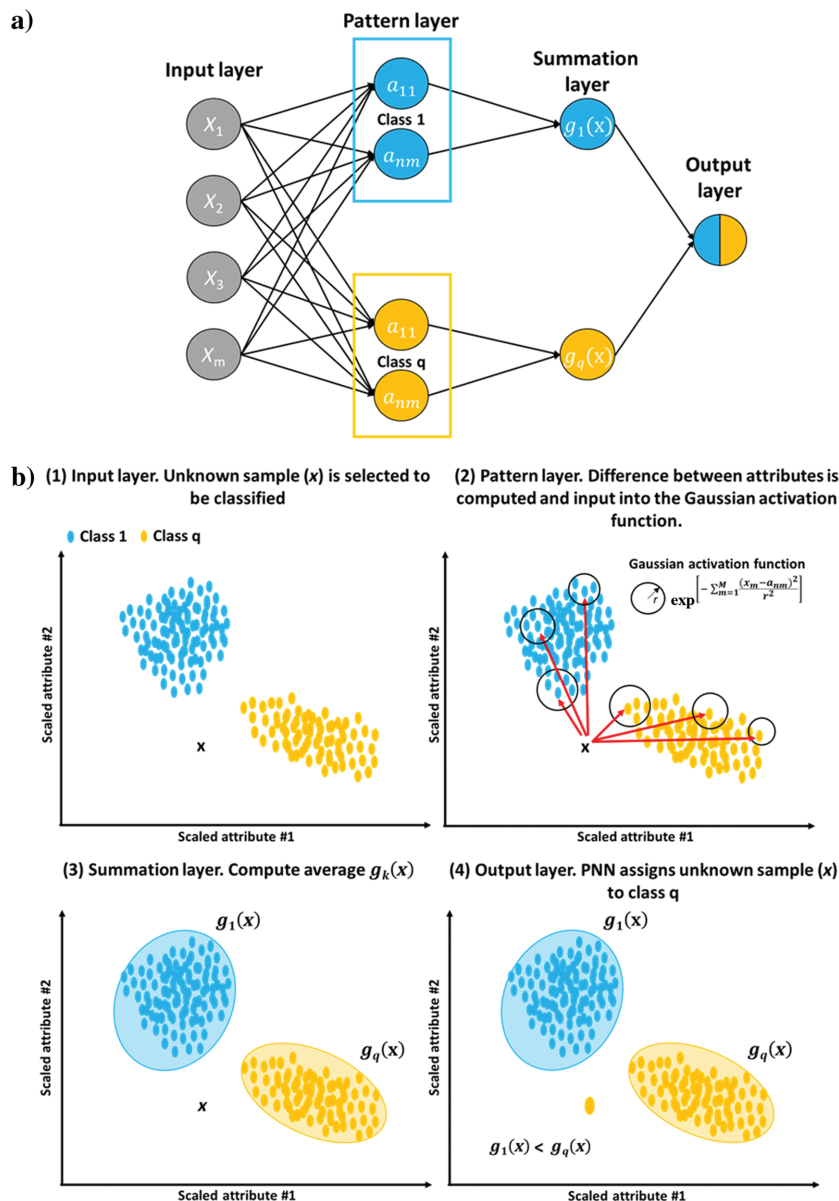


Figure 2. PNN framework (a). The PNN is composed of four layers: the (1) input layer, (2) pattern layer, (3) summation layer, and (4) output layer. (b) First, an unlabeled sample \mathbf{x} is selected for classification. The PNN computes the difference between the input sample and the training attributes \mathbf{a} and applies a Gaussian activation function. Finally, the average estimated density function $g_k(\mathbf{x})$ for each class is computed, and the unlabeled sample \mathbf{x} is assigned to the class where $g_k(\mathbf{x})$ is maximum.

PNN training

To optimize the smoothing parameter r , we sweep over a range of values for r and select the one associated with the minimum continuous error function $e_k(\mathbf{x})$ defined by Masters (1995) as

$$e_k(x) = [1 - P_k(x)]^2 + \sum_{j \neq k} [P_j(x)]^2. \quad (4)$$

Because we are interested in the error of all the samples, we define the global error as

$$E = \frac{1}{H} \sum_{h=1}^H e_k(\mathbf{x}_h), \quad (5)$$

where H is the number of validation samples.

A limitation of the sweeping over values of the smoothing parameter r is that it uses the same value for each seismic attribute. To adapt the selection of r for each attribute, we use an adaptive learning rate first-order gradient stochastic optimization algorithm called Adam, which computes the first and second moments of the gradient of E with respect to the smoothing parameter r (Kingma and Ba, 2015). For more information on the mathematical details of the Adam procedure, please refer to Appendix A.

Exhaustive PNN workflow

We present a novel technique called exhaustive PNN, which uses a PNN-based architecture and a voxel-type classification for the model generation to automatically determine the best suite of seismic attributes for performing a supervised seismic facies classification.

The first step in the exhaustive PNN workflow (Figure 3) consists of selecting a suite of candidate seismic attributes using our geologic insight. Using $M = 7$ candidate input attributes, the total number of combinations is $2^M - 1 = 127$. Then, we apply a 3D Kuwahara filter to block and smooth the seismic attributes, preconditioning them for subsequent classification (Qi et al., 2016). Second, a group of polygons for each facies is selected to create the training and validation data sets used for the model generation. In this application, supervised data labeled by the interpreter represent 0.0093% of the seismic volume after picking the polygons for each seismic facies on seven

coarsely spaced inlines. Then, these data were split into two parts, with 80% of the voxels belonging to the training data, and the remaining 20% of the voxels belonging to the validation data set.

In addition, to avoid any bias related to different units between the input candidate attributes, an attribute scaling scheme is required. In general, seismic attributes are characterized by super-Gaussian distributions (Walden, 1985; Honorio et al., 2014; Lubo-Robles and Marfurt, 2019), whereas other attributes such as Sobel filter similarity and spectral magnitude components show a Poisson distribution. Therefore, instead of using a Z-score normalization in which a Gaussian distribution is assumed, we scale our data using estimators that are robust in the presence of outliers (Huber, 1981) and do not assume knowledge of the distribution. In this study, we perform a robust scaling, in which the data are centered using the median and scaled using the interquartile range (IQR) given by the difference between the 75th and 25th percentiles. The robust scaling percentiles are computed from the training data and are used to scale the training and validation data sets.

We define an initial seismic attribute combination and smoothing parameter r to initialize the exhaustive PNN algorithm. To select the best smoothing parameter r , we sweep through values ranging from $0.05 \leq r \leq 3.5$ with an interval $\Delta r = 0.05$ and we use equation 5 to compute the validation $E_V(r)$ and training $E_T(r)$ errors. These errors are stored, and a new seismic attribute combination is defined. A smoothing parameter r is computed for each of the 127 possible attribute combinations, which are ranked based on their validation error (E_V), and then we interpret these results and select the optimal combination of seismic attributes and smoothing parameter r that provides the smallest validation error, while maintaining a balanced bias-variance trade-off.

In PNN, the training data set is used to construct the pattern layers (or a weighted combination of attributes) that will later be “learned” by the algorithm in the training step. The validation error (E_V) is computed when considering the validation data set in the input layer, whereas the training error (E_T) is calculated when comparing the training data set with itself.

At this point, our exhaustive search algorithm only allows training of the neural network using the same smoothing parameter r for each seismic attribute. To relax this restriction, we can implement an optional step that further minimizes the validation error on the

best combination by using the Adam optimization technique (Kingma and Ba, 2015) (Appendix A). Once trained and validated, we apply the PNN classifier to the optimum set of attributes and compute the probability of each class.

Bias-variance trade-off

In ML, interpreters face a bias-variance trade-off in which they need to create a model that provides an accurate prediction of the data at hand, but that is general enough to classify new data (Briscoe and Feldman, 2011; Goodfellow et al., 2016).

Briscoe and Feldman (2011) find that high-variance models are associated with overfitting whereby the classifiers fit the training data very well but lose generalization performance. In contrast, high-bias models cannot correctly capture the patterns found in the training data, thus leading to underfitting.

To find a balanced bias-variance trade-off, we analyze the relationship between the classifier’s error when evaluating our training and validation data sets. In general, underfitting is associated with relatively high

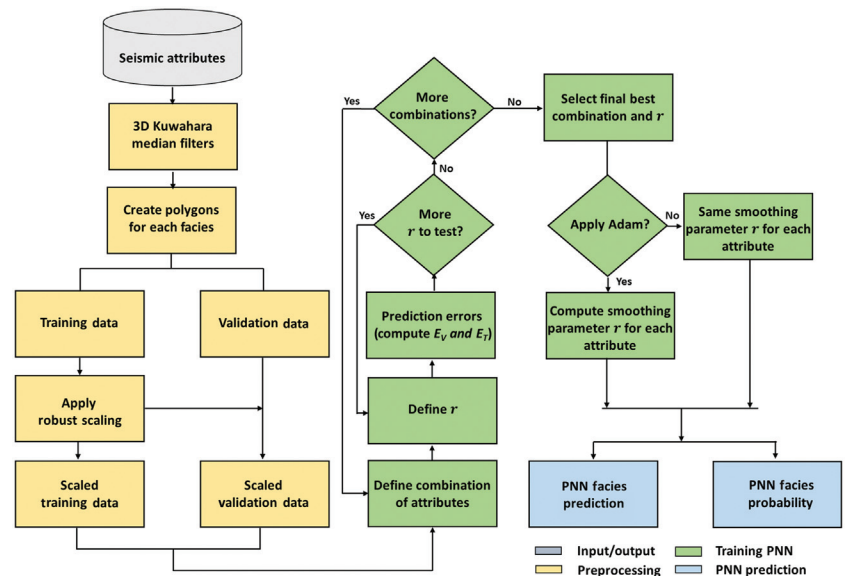


Figure 3. Exhaustive PNN workflow. First, we select a suite of candidate seismic attributes based on our geologic insight and experience. Also, a 3D Kuwahara filter is applied to block and smooth the seismic attributes’ response (Qi et al., 2016). Next, we generate the training and validation data sets by manually selecting a suite of polygons enclosing each target seismic facies. Moreover, a robust scaling scheme is applied to avoid any bias associated with different units between the seismic attributes. Then, we perform an exhaustive search and test all possible combinations of seismic attributes with the smoothing parameter r ranging from 0.05 to 3.5 and $\Delta r = 0.05$. These combinations are ranked based on their validation error (E_V), and the best combination of seismic attribute and smoothing parameter r is given by the smallest E_V while maintaining a balanced bias-variance trade-off. As an optional step, a first-order gradient optimization technique called Adam (Kingma and Ba, 2015) can be applied to the best combination to relax the fixed smoothing parameter r condition imposed by the exhaustive search algorithm and further minimize the validation error. Finally, using the exhaustive PNN attribute subset, we perform our supervised seismic facies classification, and we compute the probability of each class, which measures the confidence in the classification.

training and validation errors, whereas overfitting is characterized by a gap between the training and validation errors in which the former decreases during training, but the latter increases after finding a minimum value associated with the best generalization performance (Jabbar and Khan, 2015; Goodfellow et al., 2016).

Candidate seismic attributes

Seismic attributes are powerful tools that allow interpreters to better visualize geologic features of interest as well as to quantify reservoir properties such as continuity and morphology to study the structural and depositional setting of a particular environment (Chopra and Marfurt, 2007).

To perform the supervised seismic facies classification to differentiate between salt and nonsalt facies in the Eugene Island seismic volume, we evaluate seven candidate seismic attributes selected based on our geologic insight and past experience: coherence, gray-level cooccurrence matrix (GLCM) contrast, GLCM dissimilarity, total energy, energy deviation, covariance of dip and energy gradient, and dip deviation. These seven candidate attributes serve as the input to our exhaustive PNN algorithm with the goal of finding the best subset combination of the seven seismic attributes and the corresponding smoothing parameter r .

The coherence attribute provides a measure of similarity between neighborhood traces, and it is widely

used by seismic interpreters to map discontinuities in the seismic data such as faults and channels edges (Chopra and Marfurt, 2007; Li and Lu, 2014) as well as low-energy, discontinuous reflectors associated with salt and shale diapirs (Chopra and Marfurt, 2007). The total energy attribute measures the sum of the energy of the neighborhood analytic traces in which geologic features associated with low-amplitude, chaotic reflectors are characterized by low coherent energy.

GLCM or texture attributes analyze lateral and vertical changes in seismic amplitudes, allowing the delineation of geologic features that are characterized by complicated patterns or textures (Haralick et al., 1973; Angelo et al., 2009). In this paper, we compute two GLCM attributes: GLCM contrast, which calculates the local intensity variation between data samples (Chopra and Marfurt, 2007; Di and Gao, 2017), and GLCM dissimilarity, which also measures the intensity variation between samples but is less sensitive to outliers than GLCM contrast.

Nonparallelism attributes (Qi and Marfurt, 2019) provide the standard deviation of structural dip and amplitude gradients within an analysis window. The energy gradient measures how the seismic energy varies laterally along the structural dip, whereas the dip deviation attribute computes changes from parallel to chaotic reflections. The covariance of the dip and energy seismic attribute is sensitive to highly chaotic, rotated, and high-

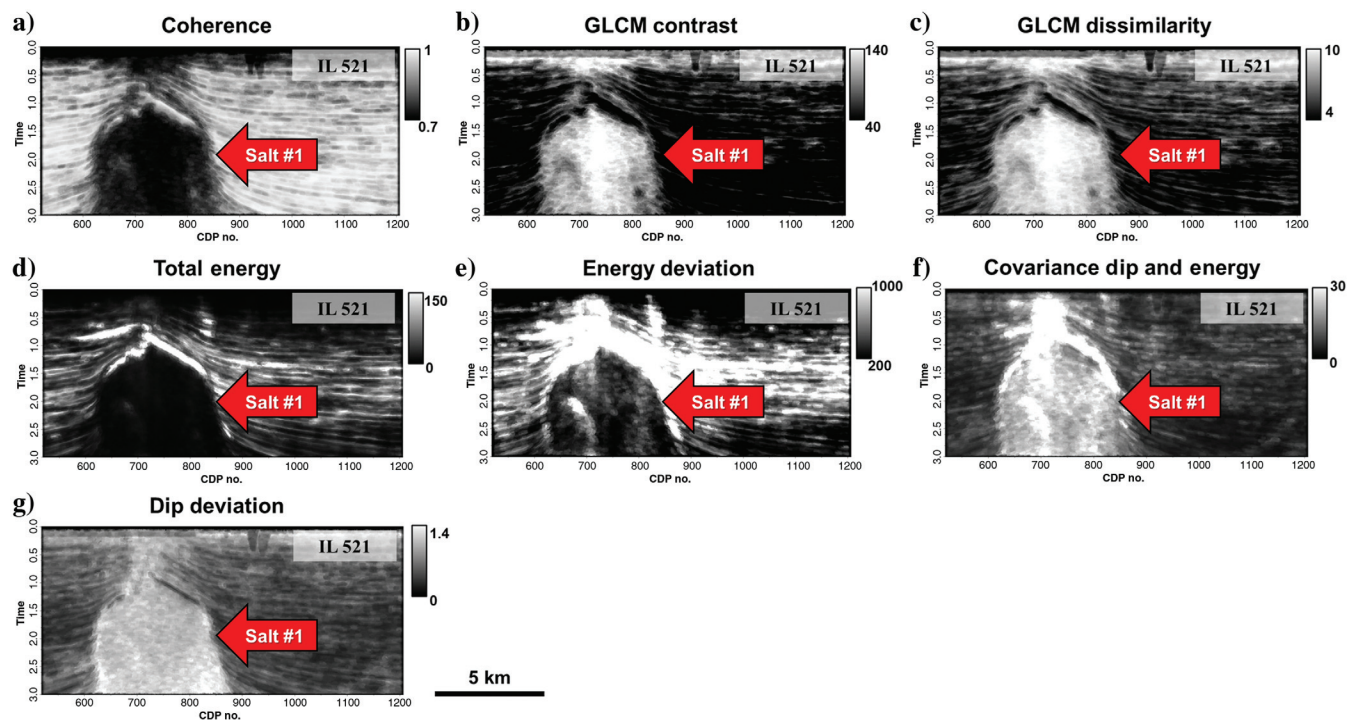


Figure 4. Candidate attributes to be used as input in the exhaustive search algorithm selected based on our geologic insight. (a) Coherence, (b) GLCM contrast, (c) GLCM dissimilarity, (d) total energy, (e) energy deviation, (f) covariance dip and energy, and (g) dip deviation. The selected candidate attributes show different responses when comparing the salt diapir (the red arrow) against the more coherent, higher amplitude background geology. A 3D Kuwahara filter (Qi et al., 2016) is applied to smooth the internal response and sharpen the edges of the salt diapir to improve the discrimination between salt and the nonsalt seismic facies during classification.

amplitude deformed reflectors. Conformal sediments are characterized by similar dips in an analysis window, MTD and karst collapse exhibit greater variability, whereas the “reflectors” within salt are a mix of coherent and random noise, giving rise to rapidly changing dips and amplitude gradients.

In Figure 4, we show the 3D Kuwahara-filtered seismic attributes along inline 521. We note that the selected candidate attributes show different responses when comparing the salt diapir (the red arrow) against the more coherent, higher amplitude background geology. Moreover, we observe that applying a Kuwahara filter using 3D overlapping oblique cylindrical windows aligned with the average structural dip smooths the internal seismic response of salt diapir 1 and sharpens its edges, thus improving the discrimination between salt and the nonsalt seismic facies.

Definition of training and validation data sets

To generate a PNN model to isolate the salt diapirs present in the Eugene Island data set from the background geology, we need to define our training and validation data sets. As training data, we pick a suite of polygons for inline 501 to 551 at 10-line intervals (Figure 5a–5f) to extract the voxels of the salt (the purple polygon) and nonsalt (the green polygon) seismic facies from the seven seismic attributes used as input in the exhaustive PNN workflow. For the validation data

set, we only pick a suite of polygons enclosing the salt (the purple polygon) and nonsalt (the green polygons) facies along inline 451 (Figure 5g). These training and validation data sets consist of approximately 28,500 and 5500 voxels, respectively, thus maintaining an approximate 80%–20% splitting ratio for training the PNN.

Note that the training and validation sets are generated only for salt diapir 1 to leave salt diapir 2 as testing data (Figure 1) to evaluate the performance of the PNN when classifying new unlabeled (unseen) data. In addition, no time slices are used when generating these data sets to avoid any data leakage from the validation to the training data set. In practice, we suggest using those inlines that best exhibit the variability in the data volume.

Results

Attribute selection to discriminate salt from the background geology in the Eugene Island seismic volume using exhaustive PNN

After we select the candidate seismic attributes to be used as input in the exhaustive PNN algorithm (Figure 4) and generate the training and validation data sets defining the salt and nonsalt seismic facies (Figure 5). We apply a robust scaling to change the units of the seismic attributes to a common scale to avoid any bias that can affect the prediction accuracy of the model.

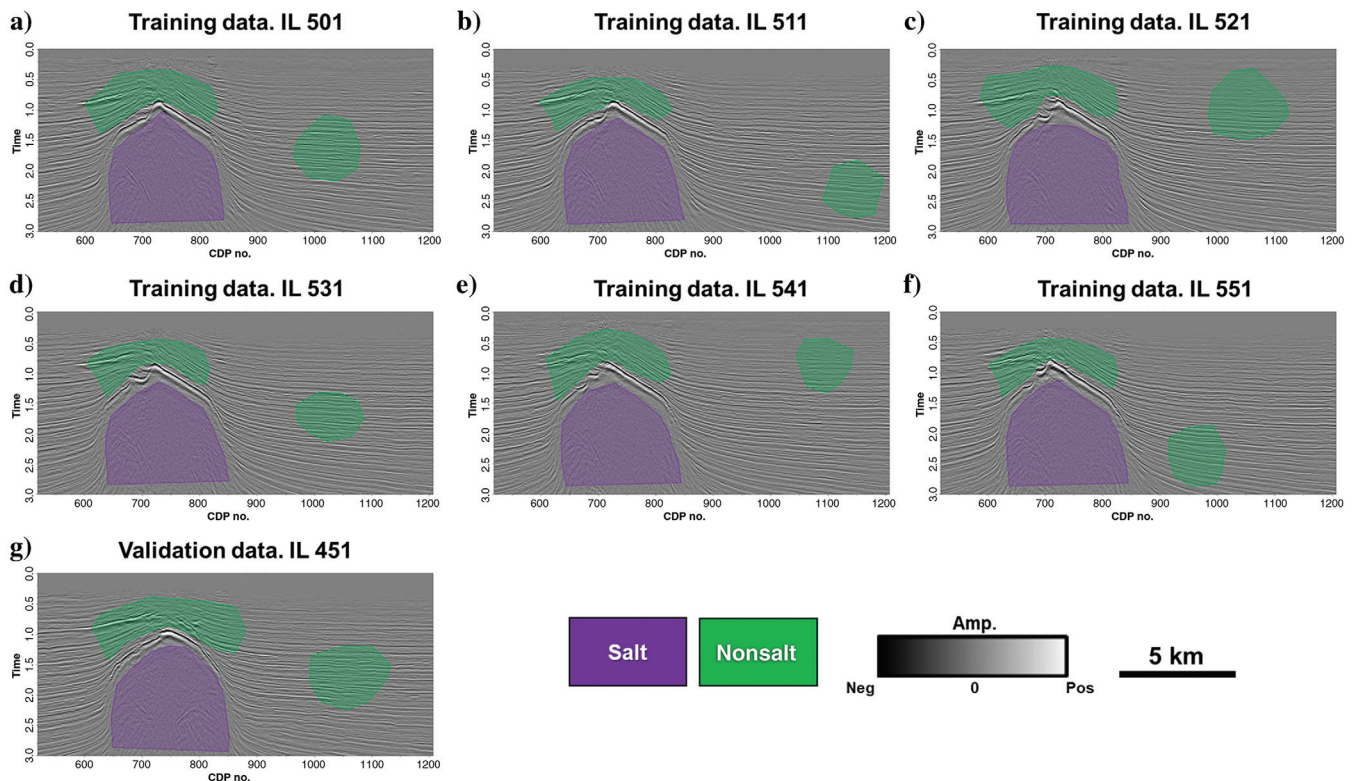


Figure 5. Training and validation data sets definition. (a–f) The training data sets consist of a suite of manually picked polygons from inline 501 to 551 with a 10 inline interval enclosing the salt (the purple polygons) and nonsalt seismic facies (the green polygons). (g) Validation data set enclosing the target facies along inline 451.

In Figure 6, we show the histograms of the training data set before (Figure 6a) and after (Figure 6b) applying robust scaling to all of the input features. We observe that the shape of the distributions is maintained after scaling and that all input features have a similar range. Moreover, input features such as the coherence, GLCM contrast, GLCM dissimilarity, covariance dip and energy, and dip deviation are characterized by a bimodal distribution, whereas the total energy and energy deviation are associated with a skewed distribution. Applying the robust scaling results in a better scaling scheme than a Z-score normalization that assumes a normal distribution of the data.

Observe that the shape of the distributions is maintained after applying the robust scaling percentiles computed from the training data set to the validation samples (Figure 7). Also note that the candidate attributes for the training and validation data sets show very similar distribution meaning that we are capturing the

same intrinsic patterns on both data sets, which the PNN “learns” to distinguish between salt and nonsalt seismic facies in the Eugene Island seismic survey.

When running the exhaustive PNN algorithm using seven input candidate attributes, we test 127 different combinations between the attributes. We then store the ideal smoothing parameter r associated with the best validation (E_V) and training (E_T) errors to make a low-bias–low-variance model able to generalize when classifying the remaining unlabeled data. Also, in this application, we compute a suite of evaluation measures given by the accuracy, precision, recall, specificity, and the area under the received operating characteristic (ROC) curve to further assess the performance of the combinations (Lachiche and Flach, 2003; Fawcett, 2004; Sokolova et al., 2006; Sokolova and Lapalme, 2009).

Performance evaluation metrics are constructed from the confusion matrix in which correctly classified and misclassified samples for each class are stored and divided into the true-positive, true-negative, false-positive, and false-negative categories (Sokolova et al., 2006; Sokolova and Lapalme, 2009). In this study, the positive and negative classes are associated with the salt and nonsalt seismic facies, respectively.

Following Sokolova et al. (2006) and Sokolova and Lapalme (2009), the accuracy estimates the global performance of the classifier without considering a specific class, whereas precision and recall compute how often the model correctly classified the positive class. Precision is defined as the ratio of true positives to the total number of samples predicted as positive, and recall is calculated as the true positives divided by the total number of samples actually belonging to the positive class. Finally, specificity determines the efficacy of the model in identifying the negative class and is computed as the fraction of true negatives to the sum of true negatives and false positives (Sokolova et al., 2006; Sokolova and Lapalme, 2009).

The ROC curve is another technique for studying the performance of a classifier in which the relationship between the recall (true-positive rate) and the specificity (true-negative rate) is analyzed at different probability thresholds (Lachiche and Flach, 2003; Fawcett, 2004; Sokolova et al., 2006). Computing the area under the ROC curve (AUC) provides an estimate of the average performance of the ROC curve into a single value. In general, AUC values range from 0.5 (random guessing; bad perfor-

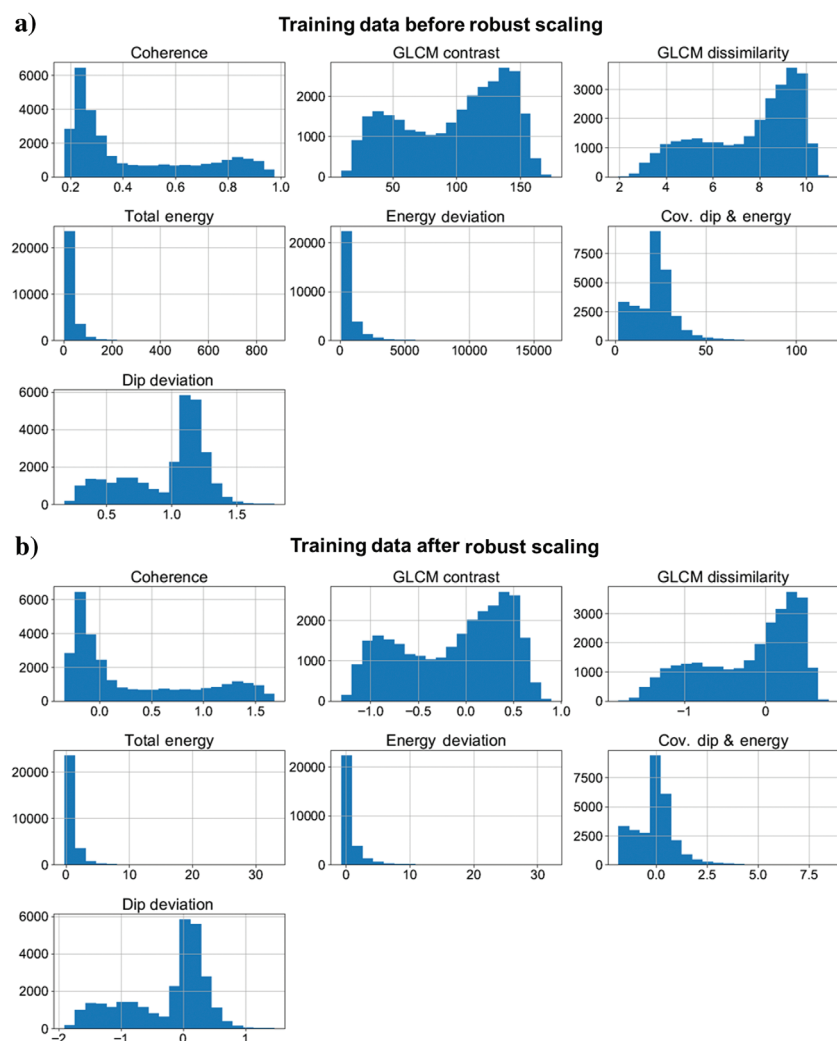


Figure 6. Histograms of the training data set (a) before and (b) after robust scaling. The shape of the distributions is maintained after scaling. Candidate attributes show non-Gaussian distributions. Therefore, a robust scaling scheme represents a better approach than Z-score normalization.

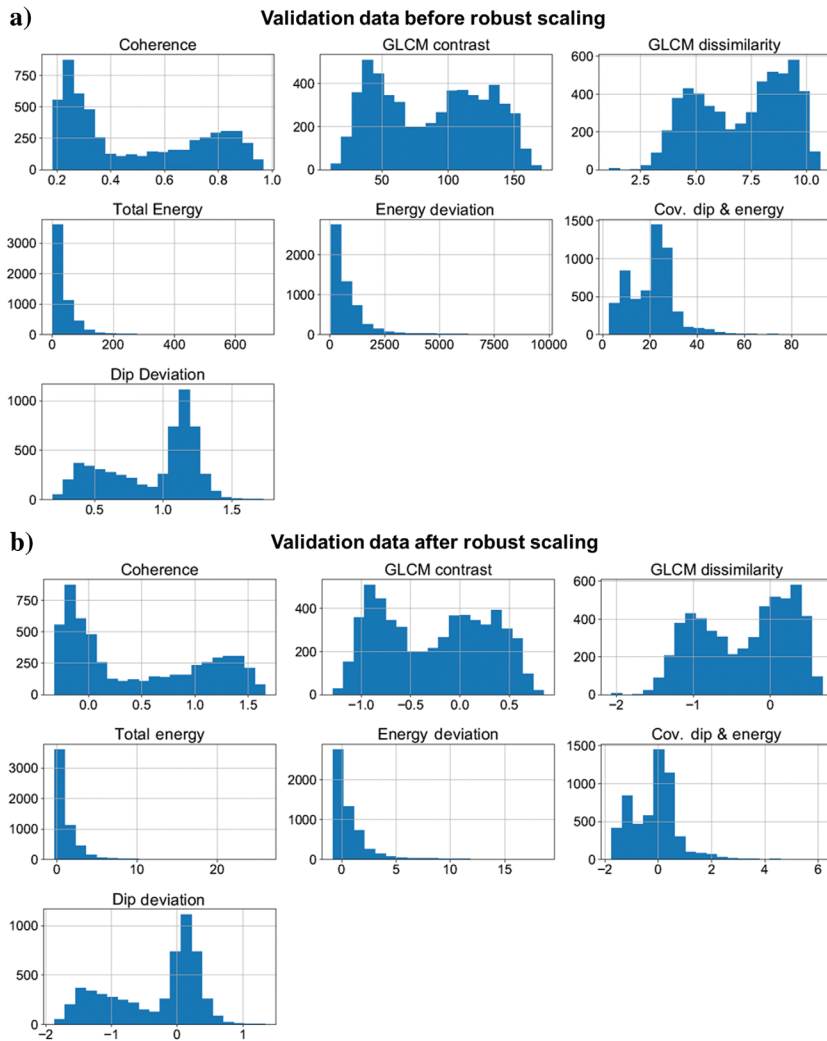


Figure 7. Histograms of the validation data set (a) before and (b) after robust scaling. The shape of the distributions is maintained after robust scaling. Distributions of the candidate seismic attributes in the training and validation data sets are very similar; thus, the same intrinsic patterns are captured on both data sets.

Table 1. The five best combinations of seismic attributes obtained after running and interpreting the results from the exhaustive PNN algorithm testing a suite of smoothing parameters ranging from $0.05 \leq r \leq 3.5$ with $\Delta r = 0.05$. These combinations show performance evaluation metrics greater than 98% associated with excellent classifiers. We select combination 1 composed of coherence, GLCM contrast, total energy, and dip deviation attributes, and we select smoothing parameter $r = 0.1$ as the best combination because it has the minimum validation error (E_V), a balanced bias-variance trade-off, and excellent performance evaluation metrics.

Combination	Attributes	r	E_V	E_T	Accuracy (%)	Precision (%)	Recall (%)	Specificity (%)	AUC
1	Coherence, GLCM contrast, total energy, and dip deviation.	0.1	0.01689	0.01223	98.91	98.45	99.48	98.3	0.9985
2	Coherence, GLCM contrast, GLCM dissimilarity, total energy, and dip deviation.	0.1	0.01693	0.0109	98.93	98.45	99.51	98.3	0.9984
3	Coherence, GLCM contrast, total energy, energy deviation, and dip deviation.	0.15	0.01712	0.01167	98.93	98.35	99.62	98.19	0.9985
4	Coherence, GLCM dissimilarity, total energy, and dip deviation.	0.1	0.01723	0.01261	98.93	98.48	99.48	98.3	0.9985
5	Coherence, GLCM contrast, GLCM dissimilarity, total energy, energy deviation, and dip deviation.	0.15	0.01724	0.01058	98.89	98.31	99.6	98.15	0.9984

mance) to 1.0 (excellent performance) (Fawcett, 2004).

In Table 1, we show the five best combinations of seismic attributes obtained after running and analyzing the results from the exhaustive PNN algorithm testing a suite of smoothing parameters ranging from $0.05 \leq r \leq 3.5$ with $\Delta r = 0.05$. We note that these combinations of attributes show values of accuracy, precision, recall, specificity, and AUC greater than 98% representing excellent performance when distinguishing between salt and nonsalt seismic facies.

Also, the minimum validation error (E_V) in combinations 1, 2, and 4 was obtained using a smoothing parameter $r = 0.1$, whereas combinations 3 and 5 obtained better performance when using a smoothing parameter of $r = 0.15$ because there is an increase in the gap between the training and validation errors associated with overfitting of the model when using smaller values of r .

When analyzing combinations 1, 2, and 3, we select combination 1, which is composed of the coherence, GLCM contrast, total energy, and dip deviation attributes, and we select smoothing parameter $r = 0.1$ as the best combination for differentiating between salt and nonsalt facies in the Eugene Island seismic survey because, using only four seismic attributes, it provides the minimum validation (E_V) error and a balanced bias-variance trade-off. Moreover, this combination shows excellent

performance during the classification associated with high values of accuracy, precision, recall, specificity, and AUC.

In Figure 8a, we show the learning curve associated with combination 1. We observe that using values of $r > 0.1$ results in relatively high training (E_T) and validation (E_V) errors possibly associated with the model underfitting the data. In contrast, when the smoothing parameter is equal to $r = 0.05$, E_T and E_V change from 0.01223 and 0.01689 to 0.00324 and 0.02032, respectively. This rapid decrease in E_T and increase in E_V indicates that the model is overfitting the data leading to a decrease in performance when classifying new unseen data. In Figure 8b, we show the ROC curve for combination 1, where the diagonal blue line represents a random guess classifier that does not have information to distinguish between facies (Fawcett, 2004). We note that combination 1 shows a high true-positive rate, a low false-positive rate, and an AUC close to 1.0, indicating that the model can correctly differentiate between salt from nonsalt seismic facies.

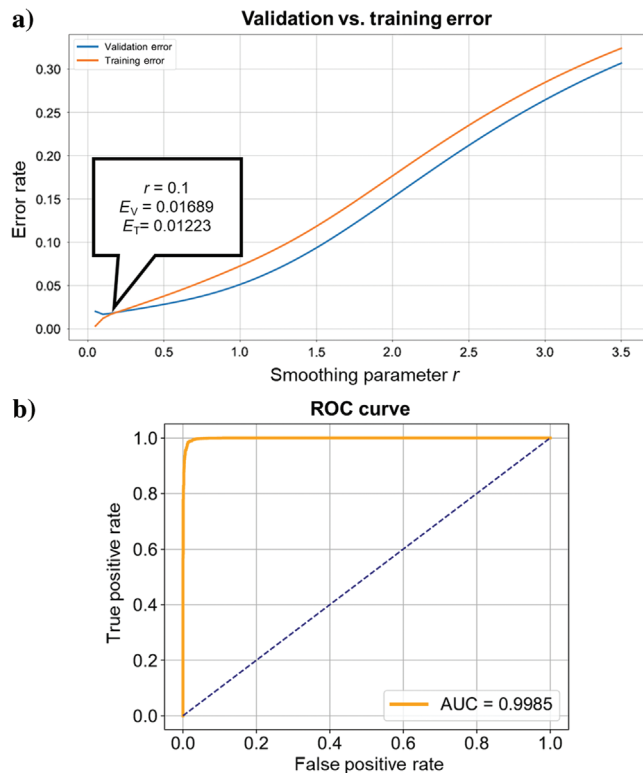


Figure 8. (a) Learning curve of combination 1 composed of the coherence, GLCM contrast, total energy, and dip deviation attributes. The ideal smoothing parameter is given by $r = 0.1$. For $r \geq 0.1$, the training (E_T) and validation (E_V) errors are high, possibly implying underfitting. When $r = 0.05$, there is a rapid decrease in E_T and an increase in E_V , suggesting overfitting. (b) ROC curve for combination 1. The diagonal blue line represents a random guess classifier that does not distinguish between facies correctly (Fawcett, 2004). Combination 1 shows an AUC close to 1.0 and high true-positive and low false-positive rates implying that the classifier can correctly distinguish salt from the background geology.

In Figure 9, we show the results obtained after applying the exhaustive PNN using the coherence, GLCM contrast, total energy, and dip deviation attributes and the smoothing parameter r equal to 0.1 to the Eugene Island survey. The PNN facies prediction corendered with the seismic amplitude along inline 391 (Figure 9a) shows that, in general, the neural network classifies correctly between the salt (purple facies; red arrow) and nonsalt seismic facies (the green facies).

However, some salt classification gaps associated with coherent migration artifacts are visible inside salt diapir 1 (the blue arrows). These features are not classified as salt because they have a different seismic pattern that is closer to those of valid reflections from the conformal sediments. In contrast, some low-amplitude discontinuities related to normal faults in the area (the yellow arrow) and missing or noisy data in the edges of the survey with little interpretational value (the red rectangle) are misclassified as salt (the purple facies). The data quality plays an important role in voxel-by-voxel classification algorithms. In contrast, a human interpreter would be able to put such features in their proper geologic and/or seismic data quality context (Posamentier and Kolla, 2003).

Figure 9b shows the PNN facies prediction corendered with the seismic amplitude volume along time slice $t = 1.78$ s. Note that the salt diapir 1 (the red arrow) is correctly classified by the exhaustive PNN algorithm. In addition, salt diapir 2 used as a test data set is also correctly classified by the proposed algorithm as salt facies (purple facies; the red arrow).

Finally, in Figure 9c and 9d, we examine the PNN salt probability volume along inline 391 and time slice $t = 1.78$ s. We observe that the extracted purple facies in salt diapir 1 and salt diapir 2 are classified as salt with very high probabilities meaning that the proposed algorithm has high performance when distinguishing between the salt and the surrounding geology.

Correlation analysis

To analyze the relationship between the candidate attributes, we evaluate their correlation heatmap using the training and validation data sets (Figures 10 and 11). To quantitatively assess their correlation, we examine the Pearson's and Spearman's rank correlations. The Pearson (1894) correlation measures the linear dependence between the features, whereas the Spearman (1904) rank correlation evaluates linear or nonlinear positive and negative relationships using a monotonic function. From Figures 10 and 11, we analyze the correlations between attribute pairs associated with combination 1 (the green rectangles). The absolute Pearson's correlation and Spearman's rank correlations vary from 0.44 to 0.95 and 0.63 and 0.97, respectively, in the training data set, whereas, in the validation data set, the absolute Pearson's correlation varies from 0.52 to 0.95 and the Spearman's rank correlation ranges from 0.73 to 0.97. We also note that the coherence attribute

has a high correlation with the GLCM contrast and dip deviation.

In Figures 10 and 11, we also note that the GLCM contrast and GLCM dissimilarity show a very high average Pearson's and rank correlations of 0.99 making them almost perfectly correlated. We note that when the exhaustive PNN uses them together (Table 1, combination 2) the validation error (Ev) of the neural network increases.

According to Guyon and Elisseeff (2003), redundant attributes are characterized by a perfect correlation; thus, adding them to an ML architecture should not provide any additional information. However, if two attributes show a very high correlation, they can complement each other to provide better class separation. Guyon and Elisseeff (2003) suggest that irrelevant attributes by themselves can be more valuable if they are combined with others. Therefore, we hypothesize that highly correlated attributes can complement each other because the performance of the classifier increases

when they are used together. Kim et al. (2019) find that using correlated attributes provided superior classifications in noisier parts of the data.

To test our hypothesis, we analyze the facies predictions using two highly correlated attributes — dip deviation and coherence, which show absolute Pearson's and rank correlations of 0.9 and 0.65, respectively. Mathematically, we know these two attributes are independent, with coherence mapping lateral changes in the waveform, and dip deviation measuring lateral and vertical changes in the dip. For the two seismic facies used in our training data — salt and conformal sediments — these two attributes are statistically correlated. To test whether using both attributes is useful, we compute the seismic facies volume using only the dip deviation and then we compare this volume with the results obtained using the dip deviation and coherence together.

From the exhaustive PNN workflow, we determined that the optimal smoothing parameter r when using only dip deviation is $r = 0.05$ because it provides the

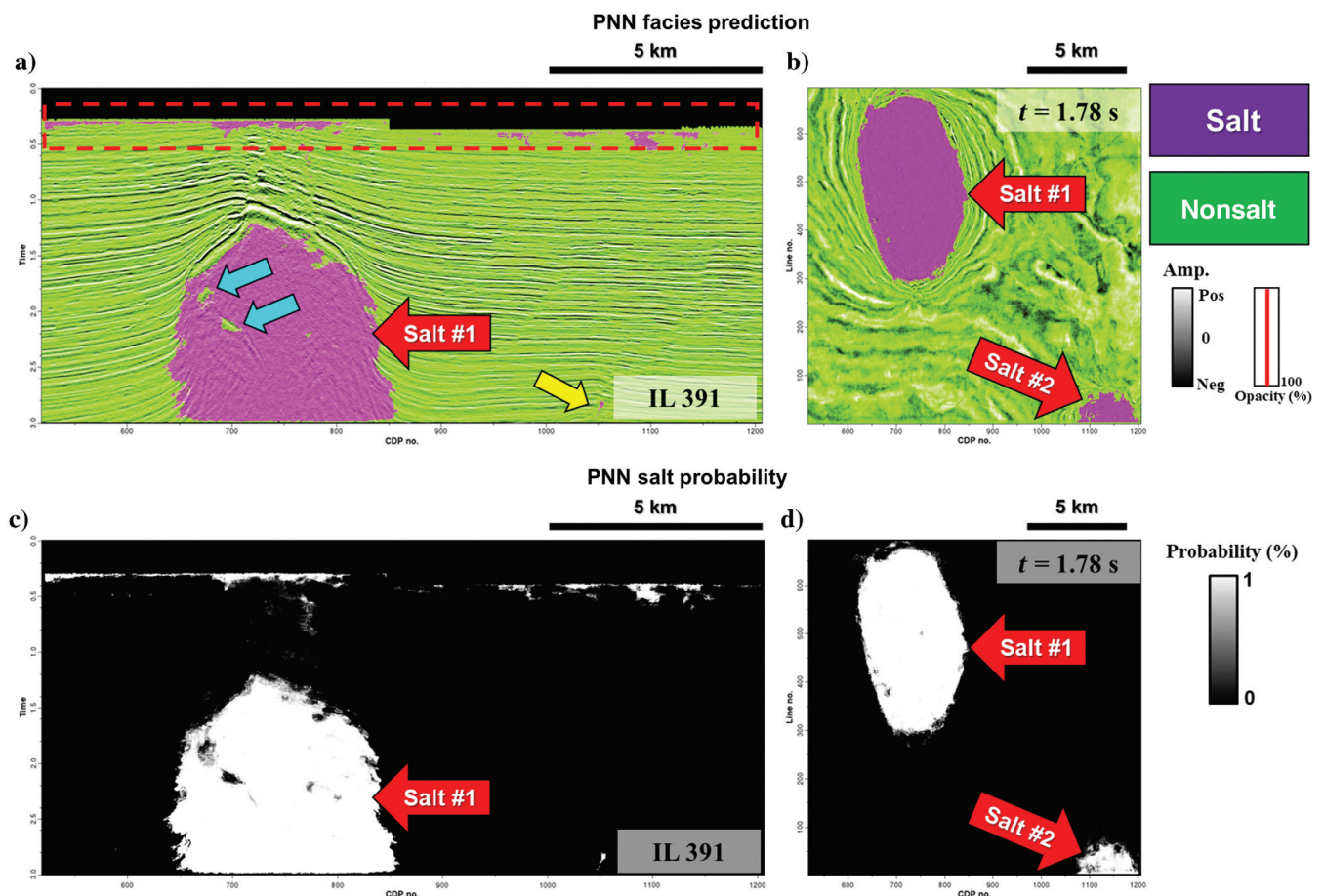


Figure 9. PNN facies prediction corendered with the seismic amplitude (a) along inline 391 and (b) at time slice $t = 1.78$ s. The PNN correctly distinguishes between salt (purple facies; red arrow) and nonsalt seismic facies (the green facies). Also, some voxels associated with coherent migration artifacts (the blue arrows), low-amplitude discontinuities related to normal faults (the yellow arrow), and missing or noisy data in the edges of the survey (the red rectangle) tend to be misclassified as salt (the purple facies). Note that salt diapir 2, which is used as a test data set, is also correctly classified as salt seismic facies by the algorithm (purple facies; the red arrow). PNN facies probability volume (c) along inline 391 and (d) at time slice $t = 1.78$ s. The extracted purple facies (salt diapirs 1 and 2) show very high probabilities associated with high performance by the model when differentiating between salt and nonsalt seismic facies.

lowest $E_v = 0.1046$, whereas when using the combination of dip deviation and coherence, the optimal r is equal to 0.2 with a validation error of $E_v = 0.029$, which represents a 72% decrease in the validation error compared to the result obtained using only the dip deviation as the input attribute. Moreover, when using only the dip deviation as input, the accuracy, precision, recall, specificity, and AUC of the classification are equal to 0.937, 0.894, 0.997, 0.872, and 0.9475, respectively, whereas while using the dip deviation and coherence we obtain accuracy = 0.983, precision = 0.979, recall = 0.988, specificity = 0.9781, and AUC = 0.9971. Therefore, the latter combination shows an increase

in the accuracy, precision, specificity, and AUC of the results.

In Figure 12a, we analyze the PNN facies prediction corendered with the seismic amplitude along inline 391 using the dip deviation as the input attribute and a smoothing parameter of $r = 0.05$. We note that the neural network does a good job of classifying the salt and nonsalt seismic facies. However, there are several gaps inside salt diapir 1 (the blue arrows) that were misclassified as nonsalt seismic facies by the algorithm. In addition, areas near normal faults (the yellow arrow) and noisy data (the red rectangle) are misclassified as salt.

Figure 12b shows the PNN facies prediction for the same line using the combination of the dip deviation and coherence attributes and the smoothing parameter $r = 0.2$. Misclassifications within the salt are reduced to one large gap (the blue arrow) corresponding to the coherent noise indicated by the blue arrow in Figure 1, whereas outside the salt, misclassifications associated with normal faults (the yellow arrow) and noisy areas near the edges of the seismic volume (the red rectangle) are diminished.

In Figure 13a and 13b, we compare the PNN facies prediction using only the dip deviation against the facies prediction volume using the dip deviation and coherence at time slice $t = 1.78$ s. We observe that when using two seismic attributes, there is a better delineation of the edges of the salt diapir 1 (the blue arrows). However, on both examples, the model tends to overestimate the size of the salt diapirs by classifying some of the surrounding conformal sediments as salt. Finally, salt diapir 2 looks better defined internally (the yellow arrows) when using the dip deviation and coherence as input attributes.

Although the dip deviation and coherence show a high correlation between each other, we observe in Figures 12 and 13 that these attributes complement each other resulting in better class separation in the multiattribute space when differentiating between salt and nonsalt seismic facies in the Eugene Island seismic survey.

Facies prediction using an optimal subset versus all candidate seismic attributes

To further assess the effectiveness of the exhaustive PNN workflow, we compare the facies prediction volume when taking all the candidate seismic attributes and the subset of attributes com-

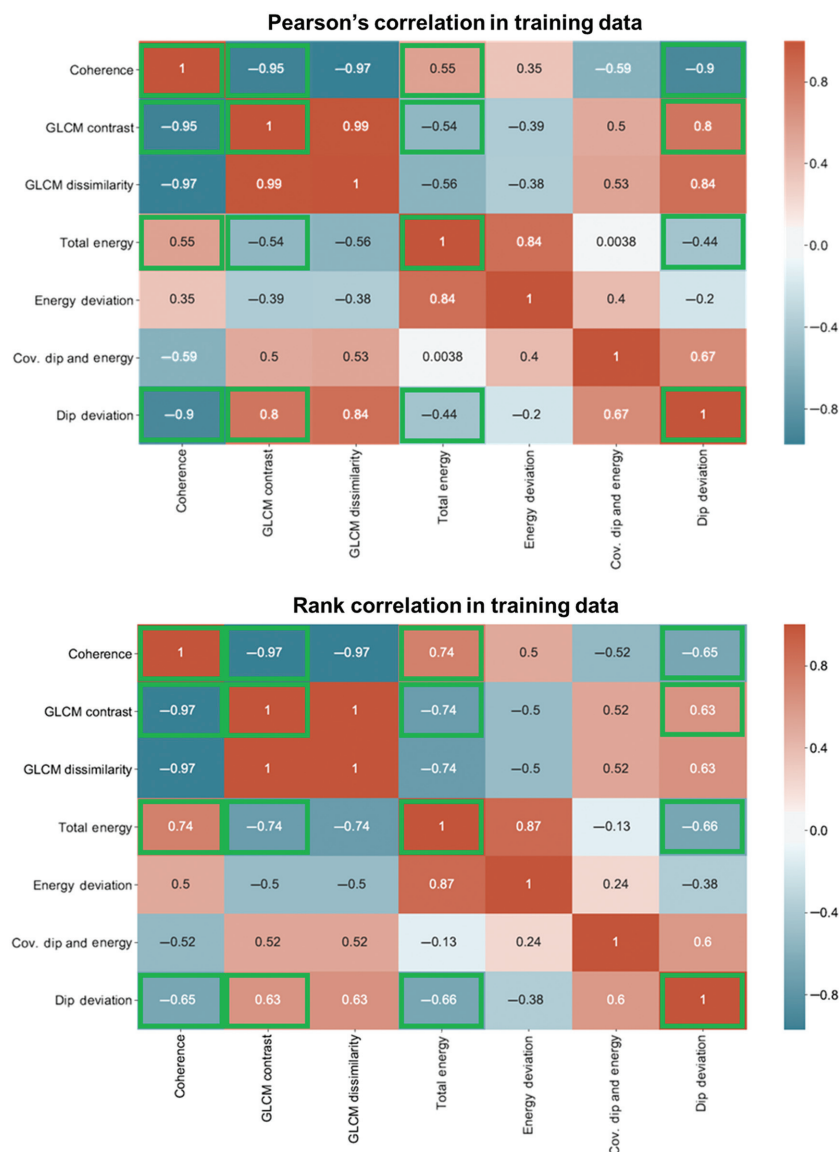


Figure 10. Correlation heat map of the training data set. The absolute Pearson's and rank correlations vary from 0.44 to 0.95 and 0.63 and 0.97, respectively, in combination 1. Note that the coherence attribute has a high correlation with the GLCM contrast and dip deviation. Following Guyon and Elisseeff (2003), we hypothesize that high correlated attributes can complement each other because using them together improves the performance of the neural networks when differentiating between salt and nonsalt seismic facies.

posed of coherence, GLCM contrast, total energy, and dip deviation as input in the neural network for performing the seismic facies classification.

In Figure 14, we show the learning curve when using all of the candidate attributes as input. We note that for $r > 0.45$, the model shows high training (E_T) and validation (E_V) errors possibly associated with underfitting, whereas when using values of $r < 0.45$, there is a large gap between the training (E_T) and validation (E_V) errors indicating that the model is overfitting the data. We hypothesize that the increasing gap between these errors might be associated with the Hughes phenomenon (Hughes, 1968) due to the increasing number of attributes used as the input.

To perform an unbiased comparison, we consider two possible cases when computing the seismic facies volume using all seven candidate seismic attributes. Case 1 consists of selecting the smallest validation error giving by $E_V = 0.01977$ and $r = 0.2$ without considering the large gap existing between the validation and training errors. Case 2 tries to minimize the gap between the training and validation errors. Here, we select $r = 0.45$ as the optimal smoothing parameter because it provides training and validation errors that are closer to each other ($E_V = 0.02325$ and $E_T = 0.02322$).

In both cases, we note that there is an increase in the validation error ranging from 14.6% to 27.4% and a decrease in the accuracy, precision, recall, and specificity compared to the results obtained using the exhaustive PNN attribute subset.

In Figure 15, we show the comparison of the PNN facies prediction volumes corendered with the seismic amplitude along inline 391 considering case 1 (Figure 15a), case 2 (Figure 15b), and the exhaustive PNN attribute subset (Figure 15c). In general, we note that salt diapir 1 shows a similar internal response and only minor changes in the edge definition (the blue arrows). Therefore, including more attributes does not provide any significant change or improvement in the facies prediction. However, cases 1 and 2 show an increase of voxels associated with normal faults (the yellow arrows) and seismic noise (the red rectangle), being misclassified as salt seismic facies compared to the results obtained using the exhaustive PNN attribute subset.

Analyzing the PNN facies prediction corendered with the seismic amplitude

volume at $t = 1.78$ s for case 1, case 2, and the attribute subset selected using the exhaustive PNN workflow (Figure 16), we still observe that salt diapir 1 does not show any significant change when including more attributes as inputs in the algorithm. However, when studying salt diapir 2, which is used as the test data set to assess the performance of the model when classifying unseen data, we note that the result obtained using the exhaustive PNN attribute subset (Figure 16c) displays a better internal result compared to the facies volumes obtained in cases 1 and 2 (Figure 16a and 16b) in which salt diapir 2 has more gaps possibly associated with coherent migration artifacts being misclassified as nonsalt seismic facies (the yellow arrows).

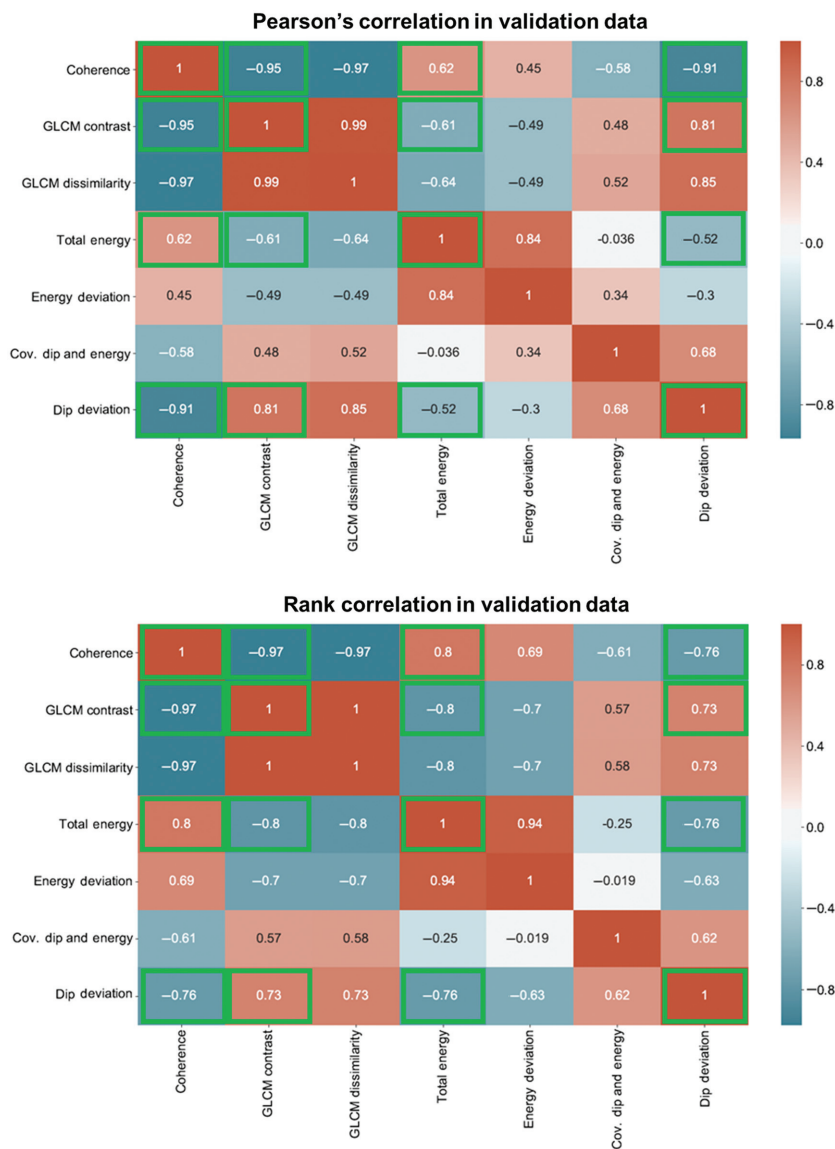


Figure 11. Correlation heat map of the validation data set. The absolute Pearson's correlation varies from 0.52 to 0.95, and the Spearman's rank correlation ranges from 0.73 to 0.97 in combination 1. Similar to the correlations obtained from the training data set, the coherence still shows a high correlation with the GLCM contrast and the dip deviation seismic attributes.

Finally, from the results obtained after applying the exhaustive PNN algorithm, we note that from seven input candidate attributes, a suite of four seismic attributes composed of coherence, GLCM contrast, total energy, and dip deviation provide the best combination to distinguish between salt and nonsalt seismic facies. We can quantitatively show that this combination generates a more robust, simpler, less computationally expensive model that avoids the Hughes (1968) phenomenon while removing irrelevant attributes that do not contribute to making a better model.

Application of the Adam optimization technique

To overcome the limitation associated with the exhaustive search algorithm in which a fixed smoothing parameter r is used, we implement an optional step in the exhaustive PNN workflow that consists of applying the Adam optimization technique to find a distinct

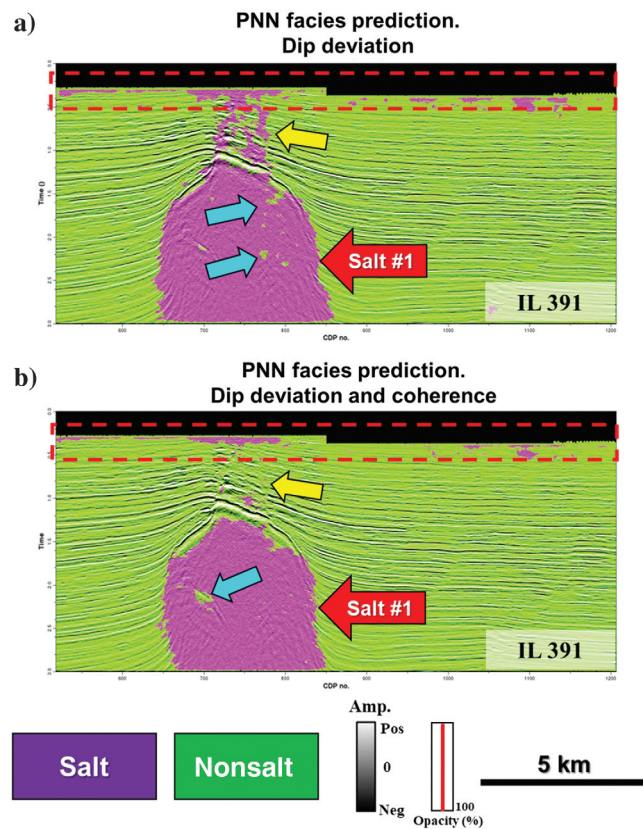


Figure 12. PNN facies prediction corendered with the seismic amplitude along inline 391 using (a) dip deviation and (b) dip deviation and coherence as the input attributes. In general, the PNN correctly classifies between salt and nonsalt seismic facies. Voxels associated with coherent noise (the blue arrows), normal faults (the yellow arrows), and noisy areas (the red rectangle) that tend to be misclassified as salt are diminished when using the combination of dip deviation and coherence as input compared to the results obtained when using only dip deviation. Note that, although the dip deviation and coherence have a high correlation, they complement each other, which results in a better seismic facies classification.

smoothing parameter for each seismic attribute for further improving the performance of the neural network when using the best combination of attributes given by the coherence, GLCM contrast, total energy, and dip deviation.

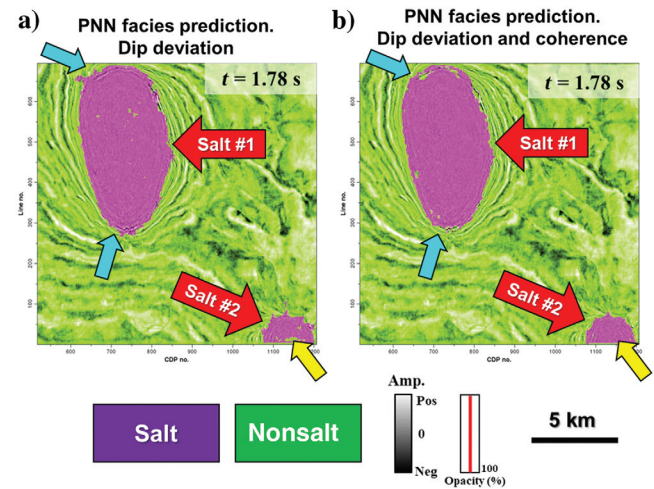
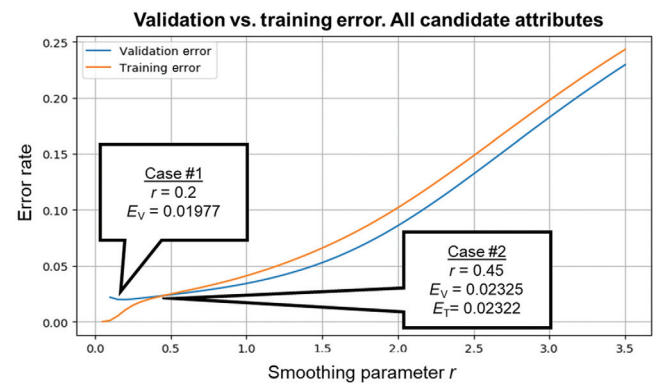


Figure 13. PNN facies prediction corendered with the seismic amplitude at time slice $t = 1.78$ s using (a) dip deviation and (b) dip deviation and coherence as input attributes. When using dip deviation and coherence as input, salt diapir 2 shows a better internal definition (the yellow arrows), whereas salt diapir 1 has a better delineation of its edges (the blue arrows). Note that on both examples, the size of the salt diapirs is overestimated because the models tend to classify some conformal sediments as the salt seismic facies.



Attributes	r	Accuracy	Recall	Precision	Specificity	AUC
All seven candidate attributes	0.2	0.9878	0.9944	0.9824	0.9807	0.9986
All seven candidate attributes	0.45	0.9856	0.9944	0.9784	0.9762	0.998

Figure 14. Learning curve when using all of the candidate attributes as input. For $r > 0.45$, the model shows high training (E_T) and validation (E_V) errors possibly implying underfitting, whereas for $r < 0.45$, there is a large gap between the errors leading to overfitting possibly related to the Hughes phenomenon (Hughes, 1968). Two cases are generated for analysis: case 1, which is associated with the smallest validation error (E_V), and case 2, which minimizes the gap between the training and validation errors.

Adam is a computationally efficient first-order gradient stochastic optimization technique that computes adaptive learning rates from the first and second moments of the gradients. Therefore, it provides robust results when facing large data sets, noisy or sparse gradients, and nonstationary problems (Kingma and Ba, 2015).

For selecting a suite of smoothing parameters r 's to be used as the starting point in the Adam optimization technique, we implement a random initialization approach to guarantee symmetry-breaking during training with values ranging from 0.05 to 0.15 because from the

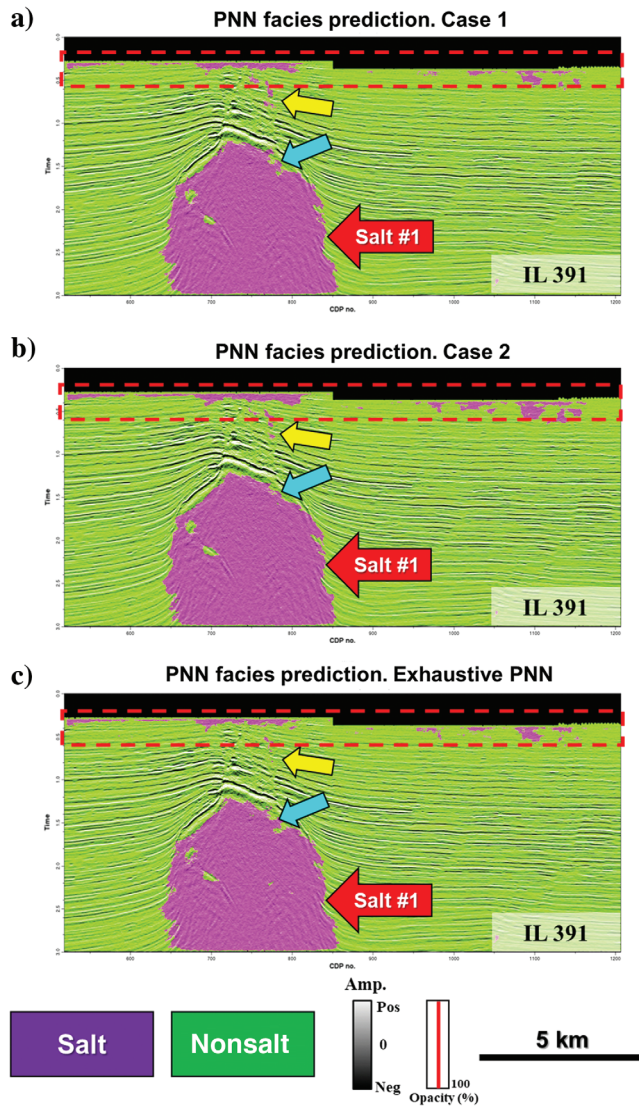


Figure 15. PNN facies prediction volumes corendered with the seismic amplitude along inline 391 for (a) case 1, (b) case 2, and (c) exhaustive PNN attribute subset used as the input. Note that including more attributes does not show any significant change or improvement in the seismic facies classification (the blue arrows). Moreover, when using the exhaustive PNN attribute subset as the input, we observe fewer voxels related to seismic noise (the red rectangle) and normal faults (the yellow arrows) being misclassified as salt.

exhaustive search algorithm we determine that a smoothing parameter close to 0.1 is providing the highest accuracy (Figure 8).

Figure 17 shows the validation error at different iterations during the implementation of the Adam algorithm. We observe that the minimum validation error (E_V) obtained is equal to 0.01627 associated with iteration 15th and smoothing parameters equal to 0.065, 0.075, 0.104, and 0.222, respectively. This new E_V is smaller than the E_V using a fixed smoothing parameter of 0.1 for all seismic attributes in combination 1. Moreover, we note an improvement in the performance evaluation metrics after implementing Adam.

Finally, we also compute the training error (E_T) using the new suite of smoothing parameters at iteration 15 (Figure 17). We observe that E_T is equal to 0.01266; thus, it guarantees that we are obtaining a balanced bias-variance trade-off model after implementing Adam.

In Figure 18, we show the results when applying the exhaustive PNN using different smoothing parameters for each seismic attribute in combination 1 after implementing Adam along inline 391. We note that the neural network is still correctly classifying between the salt

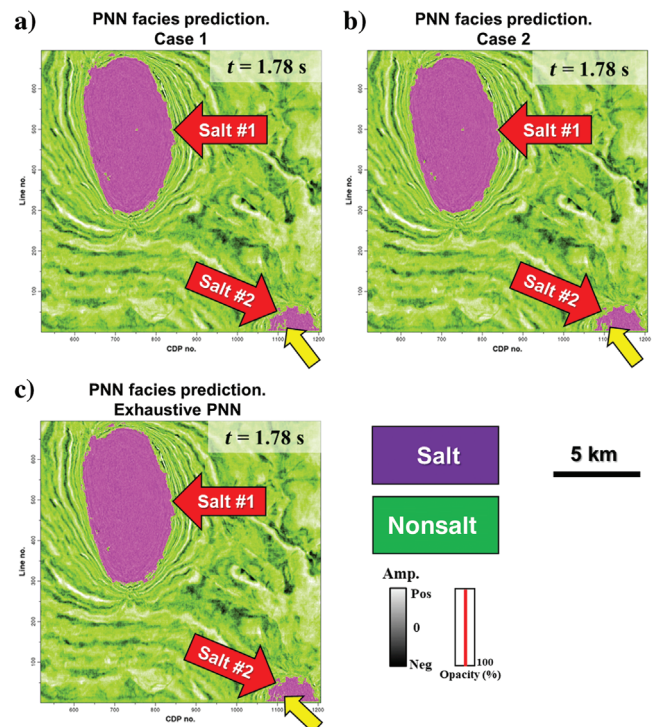


Figure 16. PNN facies prediction corendered with the seismic amplitude volume at time slice $t = 1.78$ s for (a) case 1, (b) case 2, and (c) exhaustive PNN attribute subset. Note that the results obtained using the exhaustive PNN attribute subset show a better internal definition of salt diapir 2, whereas salt diapir 1 does not show any significant change or improvement if more attributes are included. Therefore, using the exhaustive PNN algorithm, we can remove irrelevant attributes and generate a more robust, simpler classifier to perform our seismic facies classification.

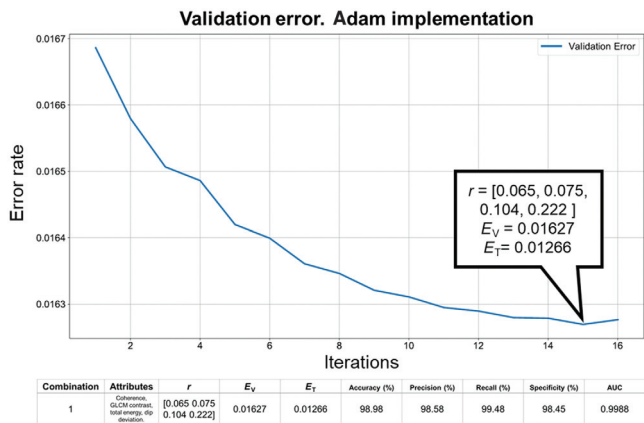


Figure 17. Validation error during the implementation of the Adam algorithm. The minimum validation error $E_V = 0.01627$ is obtained at iteration 15th and the smoothing parameters r 's equal to 0.065, 0.075, 0.104, and 0.222. Note that by relaxing the fixed smoothing parameter condition, there is a decrease in the validation error (E_V) and an increase in the evaluation metrics of the model. Finally, at iteration 15th, $E_T = 0.01266$, which guarantees a balanced bias-variance trade-off.

(purple facies; red arrow) and the background geology (the green facies). Moreover, the flanks of the salt diapir (the orange arrows) are better delineated than the results obtained when using a fixed smoothing parameter (Figure 18a). In addition, low-amplitude discontinuities related to normal faults are no longer classified as salt when applying Adam (the yellow arrow). However, gaps associated with coherent migration artifacts inside salt diapir 1 and noisy data in the edges of the survey are still misclassified by the algorithm.

In Figure 18b, we examine the PNN facies prediction after applying Adam corendered with the seismic amplitude volume along time slice 1.78 s. We observe that both salt diapirs are still correctly classified by the proposed workflow. Moreover, salt diapir 2, which is used as test data, looks better defined than when using the same smoothing parameter for each seismic attribute in combination 1.

Finally, analyzing the PNN salt probability volume along inline 391 (Figure 18c) and time slice 1.78 s (Figure 18d), we observe that the purple facies associated

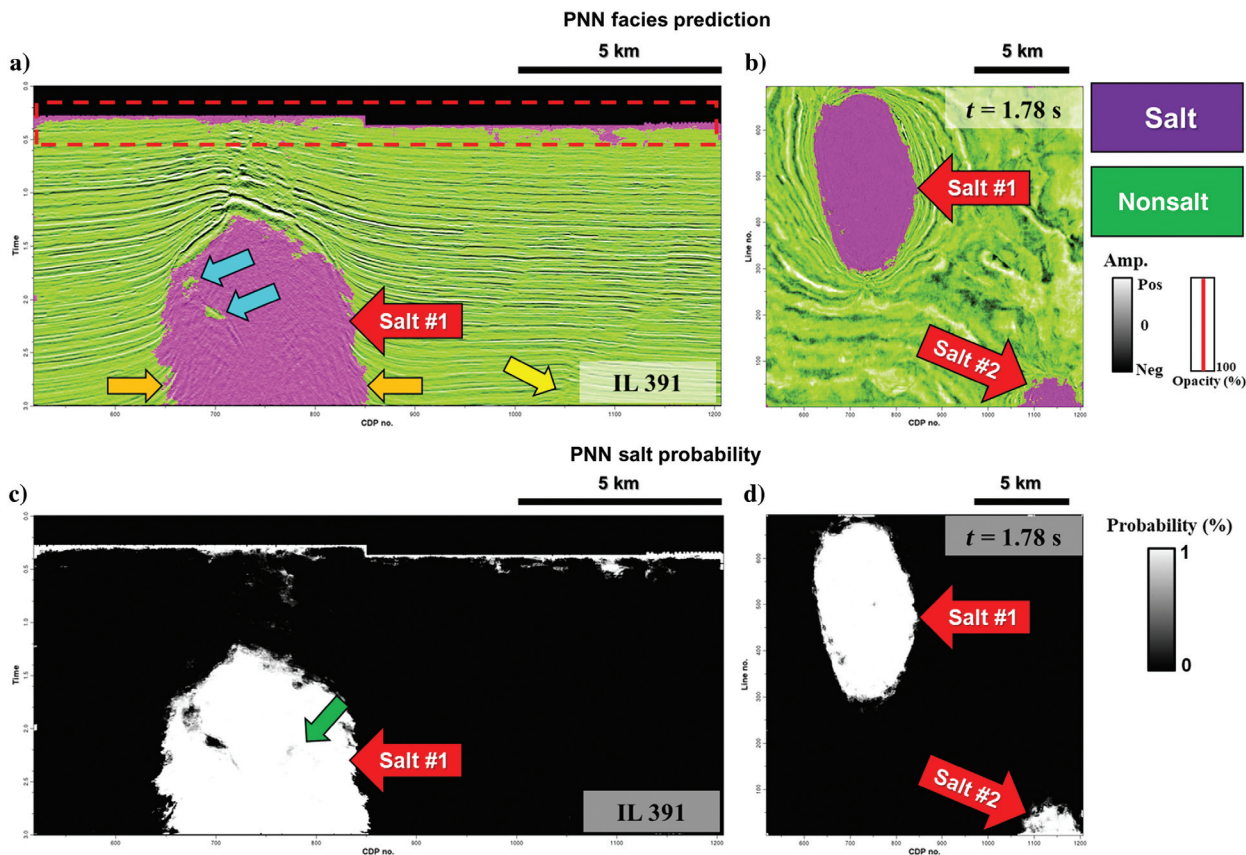


Figure 18. PNN facies prediction using Adam corendered with the seismic amplitude (a) along inline 391 and (b) at time slice $t = 1.78$ s. The PNN is still correctly classifying between salt (purple facies; the red arrow) and nonsalt seismic facies (the green facies). Flanks of salt diapir 1 are better delineated, whereas salt diapir 2, which is used as a test data set, is correctly classified and has better definition compared to the results obtained using a fixed smoothing parameter r for each seismic attribute in combination 1. However, some voxels associated with coherent noise (the blue arrows) and seismic noise toward the edges of the survey (the red rectangle) are still being misclassified as salt. PNN facies probability volume using Adam (c) along inline 391 and (d) at time slice 1.78 s. Salt diapir 1 shows an internal increase in the probabilities (the green arrow), whereas salt diapir 2 still shows high probabilities during the classification.

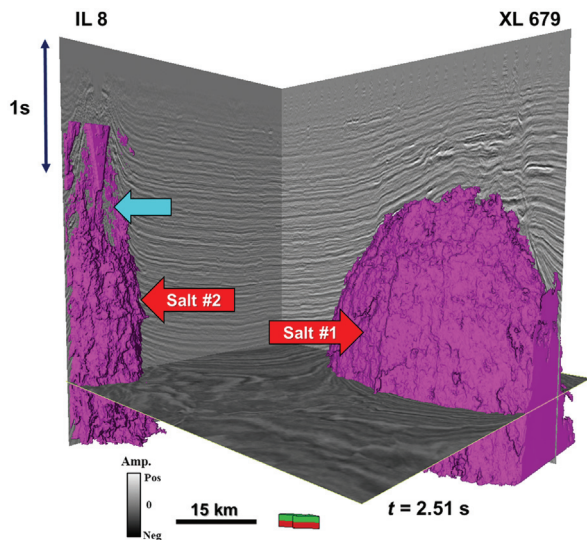


Figure 19. Geobody generation extracting salt facies from the PNN facies prediction volume with probabilities higher than 75% obtained from the PNN salt probability volume. Salt diapirs 1 and 2 (purples facies; the red arrows) are extracted with high accuracy from the surrounding conformal reflectors. However, salt diapir 2, which is used as a test data set to assess the performance of the classifier, shows some gaps (the blue arrow) possibly related to salt facies misclassified as background geology or salt voxels that show probabilities lower than 75%.

with salt diapir 1 shows an internal increase in the probabilities (the green arrow), whereas salt diapir 2 still shows high probabilities during the classification; thus, by applying Adam in the exhaustive PNN algorithm we can improve the performance of our model when differentiating between salt and nonsalt seismic facies in the Eugene Island seismic volume.

Geobody extraction

To obtain a 3D distribution of the salt diapirs present in the Eugene Island seismic survey and isolate them from the surrounding conformal reflectors, we perform a geobody extraction (Meyer et al., 2001) to model and extract the voxels from our PNN facies prediction and PNN salt probability volumes computed using the optimal combination of attributes given by coherence, GLCM contrast, total energy, and dip deviation and a suite of smoothing parameters for each of these attributes after applying Adam.

In Figure 19, we show the 3D salt mapping using as the criterion voxels characterized by salt facies with probabilities higher than 75%. We note that we are able to extract with high accuracy salt diapirs 1 and 2 (purples facies; the red arrows) from the surrounding geology. We also observe that salt diapir 2, which is used as the testing data set in this study, shows some gaps (the blue arrow), which we hypothesize are associated with misclassified salt facies as background geology or salt voxels that show probabilities lower than 75% due to the presence of crossing coherent migration artifacts.

Salt diapir 1 is well defined internally with salt voxels being classified with very high confidence (Figure 18c) by the exhaustive PNN algorithm.

Computational effort

The Eugene Island data volume used in this study consisted of 700 inlines, 700 crosslines, and 750 vertical samples, giving a total of 367.5 million voxels. The polygons constructed on the seven inlines provided 28,500 training and 5500 validation voxels. Using 60 processors on an Intel workstation, the time for the exhaustive search algorithm to find the best of 127 attribute combinations was 23.5 min. After training found the best combination to be four attributes, the final classification took 2.6 h.

Conclusion

Application of exhaustive PNN to a 3D Gulf of Mexico seismic survey proved to be a powerful tool in selecting the optimal combination of seismic attributes to perform a supervised seismic facies classification to distinguish between salt and nonsalt seismic facies. Coupling an exhaustive search algorithm together with a PNN, we determine that from seven input candidate attributes, the best combination is given by using only four attributes composed of the coherence, GLCM contrast, total energy, and dip deviation with a smoothing parameter r of 0.1. Moreover, applying a first-order gradient optimization technique called Adam, we can further improve the performance of the proposed algorithm by finding different smoothing parameters for each of the seismic attributes while maintaining a balanced bias-variance trade-off. Because a high correlation between attributes does not necessarily imply that they are redundant, and they might complement each other providing better class separation, we found that our proposed workflow can generate a simpler, more robust, less computationally expensive model by removing irrelevant attributes while maintaining attributes that can complement each other. Furthermore, the occurrence of the Hughes phenomenon is reduced after performing the attribute selection workflow. Finally, a geobody extraction is conducted to delineate the 3D distribution of the salt diapirs and isolate them from nonsalt seismic facies. Using the seismic classification results obtained from Adam and looking for voxels characterized by salt facies with probabilities higher than 75%, we extract salt diapirs 1 and 2 (the purple facies) from the surrounding geology with high accuracy. In general, salt diapir 2, used as a test data set in this study, is well-defined although some gaps are visible possibly related to misclassification or low confidence values due to the presence of crossing coherent migration artifacts. Salt diapir 1 is better internally defined than salt diapir 2 because salt voxels are classified with higher confidence by the exhaustive PNN algorithm.

Acknowledgments

We thank the U.S. National Archive of Marine Seismic Surveys, and the U.S. Geological Survey for providing the Eugene Island data set. We would also like to thank the sponsors of the Attribute-Assisted Seismic Processing & Interpretation (AASPI) consortium for their support and to Schlumberger for the licenses in Petrel provided to the University of Oklahoma. Finally, we thank H. Bedle, D. Devegowda, and V. Jayaram for their valuable comments.

Data and materials availability

Data associated with this research are available and can be accessed via the following URL: <https://walrus.wr.usgs.gov/namss/search/>.

Appendix A

Preprocessing for the exhaustive PNN algorithm

Seismic attributes often have different units of measurement and ranges of values. For example, coherence ranges from 0 to 1, whereas the seismic envelope may range between 0 and +10000, thereby requiring normalization to balance their contribution to any subsequent classification. Following Walden (1985), Honorio et al. (2014), and Lubo-Robles and Marfurt (2019), we know that, in general, seismic attributes are characterized by super-Gaussian distributions whereas other attributes such as coherence and spectral magnitude components show a Poisson distribution bias towards 0, or for coherence, bias towards 1. In this paper, we perform a simple but robust scaling that avoids knowledge of the detailed distribution and is resistant to the presence of outliers given by

$$a_m^{\text{scaled}} = \frac{a_m - q_{2m}}{q_{3m} - q_{1m}}, \quad (\text{A-1})$$

where each attribute is centered about their median q_2 and is scaled by the IQR given by the difference between q_3 and q_1 , which are the 75th and 25th percentiles. The robust scaling percentiles are computed from the training data and are used to scale the training, validation, and testing data sets.

The PNN algorithm for finding different smoothing parameters

To find a different smoothing parameter r for each seismic attribute, we need to compute the derivatives of the continuous error function with respect to the smoothing parameters (Masters, 1995). Then, using these derivatives together with a first-order optimization technique such as Adam, we update the smoothing parameters to minimize the error.

Masters (1995) computes the derivative of the error function for a single sample in the validation. In this study, we are interested in minimizing the global error E . Therefore, we generalize Masters (1995) to compute the derivative of the global continuous error E given by

$$\frac{\partial E}{\partial r_i} = \frac{1}{H} \sum_{h=1}^H \left\{ 2[P_k(x) - 1] \left[\frac{\partial P_k(x)}{\partial r_i} \right] + 2 \sum_{j \neq k} \left[P_j(x) \frac{\partial P_j(x)}{\partial r_i} \right] \right\}, \quad (\text{A-2})$$

where

$$\frac{\partial P_k(x)}{\partial r_i} = \frac{\frac{1}{N_k} \left\{ \left[2 \sum_{n=1}^{N_k} \delta_{nk} e^{-\sum_{m=1}^M \frac{(x_m - a_{nk})^2}{r_i^2}} \right] \frac{(x_i - a_{nk})^2}{r_i^2} \right\} - \left[\sum_{k=1}^K \frac{1}{N_k} \left\{ \left[2 \sum_{n=1}^{N_k} \delta_{nk} e^{-\sum_{m=1}^M \frac{(x_m - a_{nk})^2}{r_i^2}} \right] \frac{(x_i - a_{nk})^2}{r_i^2} \right\} \right] P_k(x)}{\sum_k \left[\frac{1}{N_k} \sum_{n=1}^{N_k} \delta_{nk} e^{-\sum_{m=1}^M \frac{(x_m - a_{nk})^2}{r_i^2}} \right]} \quad (\text{A-3})$$

where P represents the normalized probabilities given by the estimated density function of each class k divided by the sum of all the density functions of all classes, K represents the total number of classes, H is the number of samples in the validation data set, and δ_{nk} is the Kronecker delta function.

Then, following Kingma and Ba (2015) and using the derivative of the continuous error functions $\partial E / \partial r_i$, we apply the first-order gradient stochastic optimization algorithm called Adam that uses adaptive learning rates by computing the first and second moments of the gradients. The learning rule is given by

$$r_i^+ = r_i - \alpha \hat{m}_t / \sqrt{\hat{v}_t} + e, \quad (\text{A-4})$$

where t is the current iteration of a user-defined total number of iterations T , r_i^+ is the updated smoothing parameter for each attribute, r_i is the smoothing parameter of the previous iteration, and \hat{m}_t and \hat{v}_t are the bias-corrected first and second moment estimations of the gradient $\partial E / \partial r_i$ (equation A-2). The Adam algorithm also uses hyperparameters for the step size α and a small constant e to avoid division by zero.

With this background, the bias-corrected first and second moment estimations (Kingma and Ba, 2015) are given by

$$\hat{m}_t = \left[\beta_1 m_{t-1} + (1 - \beta_1) \frac{\partial E}{\partial r_{it}} \right] / (1 - \beta_1^t) \quad (\text{A-5})$$

and

$$\hat{v}_t = \left[\beta_2 v_{t-1} + (1 - \beta_2) \frac{\partial E^2}{\partial r_{it}^2} \right] / (1 - \beta_2^t), \quad (\text{A-6})$$

where β_1 and β_2 are also hyperparameters for the Adam algorithm. In the first iteration, $t = 0$, m_t , and v_t are initialized to zero. According to Kingma and Ba (2015), good default values for the hyperparameters are $\beta_1 = 0.9$, $\beta_2 = 0.999$, $\alpha = 0.001$, and $e = 10^{-8}$. However, in this paper, we use a step size of $\alpha = 0.01$, which results in faster convergence with a reduced number of iterations, T , needed to decrease the validation error E_V .

References

- Alexander, F., and P. Flemings, 1995, Geologic evolution of a Pliocene–Pleistocene salt-withdrawal minibasin: Eugene Island Block 330, Offshore Louisiana: *AAPG Bulletin*, **79**, 1737–1756, doi: [10.1306/7834DEEA-1721-11D7-8645000102C1865D](https://doi.org/10.1306/7834DEEA-1721-11D7-8645000102C1865D).
- Amin, A., M. Deriche, M. A. Shafiq, Z. Wang, and G. AlRegib, 2017, Automated salt dome detection using an attribute ranking framework with a dictionary-based classifier: *Interpretation*, **5**, no. 3, SJ61–SJ79, doi: [10.1190/INT-2016-0084.1](https://doi.org/10.1190/INT-2016-0084.1).
- Angelo, S. M., M. Matos, and K. J. Marfurt, 2009, Integrated seismic texture segmentation and clustering analysis to improved delineation of reservoir geometry: 79th Annual International Meeting, SEG, Expanded Abstracts, 1107–1111, doi: [10.1190/1.3255046](https://doi.org/10.1190/1.3255046).
- Barnes, A. E., 2007, Redundant and useless seismic attributes: *Geophysics*, **72**, no. 3, P33–P38, doi: [10.1190/1.2716717](https://doi.org/10.1190/1.2716717).
- Briscoe, E., and J. Feldman, 2011, Conceptual complexity and the bias/variance tradeoff: *Cognition*, **118**, 2–16, doi: [10.1016/j.cognition.2010.10.004](https://doi.org/10.1016/j.cognition.2010.10.004).
- Chang-Kai, Z., and L. Wen-Kai, 2010, Seismic attributes selection based on SVM for hydrocarbon reservoir prediction, 80th Annual International Meeting, SEG, Expanded Abstracts, 1586–1590, doi: [10.1190/1.3513144](https://doi.org/10.1190/1.3513144).
- Chopra, S., and K. J. Marfurt, 2007, Seismic attributes for prospect identification and reservoir characterization: SEG Geophysical Development Series 11.
- Chopra, S., and K. J. Marfurt, 2014, Churning seismic attributes with principal component analysis: 84th Annual International Meeting, SEG, Expanded Abstracts, 2672–2676, doi: [10.1190/segam2014-0235.1](https://doi.org/10.1190/segam2014-0235.1).
- Di, H., and D. Gao, 2017, Nonlinear gray-level co-occurrence matrix texture analysis for improved seismic facies interpretation: *Interpretation*, **5**, no. 3, SJ31–SJ40, doi: [10.1190/INT-2016-0214.1](https://doi.org/10.1190/INT-2016-0214.1).
- Di, H., M. A. Shafiq, and G. AlRegib, 2017, Seismic fault detection based on multi-attribute support vector machine analysis: 87th Annual International Meeting, SEG, Expanded Abstracts, 2039–2044, doi: [10.1190/segam2017-17748277.1](https://doi.org/10.1190/segam2017-17748277.1).
- Di, H., M. A. Shafiq, Z. Wang, and G. AlRegib, 2019, Improving seismic fault detection by a super-attribute-based classification: *Interpretation*, **7**, no. 3, SE251–SE267, doi: [10.1190/INT-2018-0188.1](https://doi.org/10.1190/INT-2018-0188.1).
- Dorrington, K. P., and C. A. Link, 2004, Genetic-algorithm/neural-network approach to seismic attribute selection for well-log prediction: *Geophysics*, **69**, 212–221, doi: [10.1190/1.1649389](https://doi.org/10.1190/1.1649389).
- Fawcett, T., 2004, ROC graphs: Notes and practical considerations for researchers: *Machine Learning*, **31**, 1–38.
- Galvis, I. S., Y. Villa, C. Duarte, D. Sierra, and W. Agudelo, 2017, Seismic attribute selection and clustering to detect and classify surface waves in multicomponent seismic data by using *k*-means algorithm: *The Leading Edge*, **36**, 239–248, doi: [10.1190/tle36030239.1](https://doi.org/10.1190/tle36030239.1).
- Goodfellow, I., Y. Bengio, and A. Courville, 2016, *Deep learning*: MIT Press.
- Guo, H., K. J. Marfurt, and J. Liu, 2009, Principal component spectral analysis: *Geophysics*, **74**, no. 4, P35–P43, doi: [10.1190/1.3119264](https://doi.org/10.1190/1.3119264).
- Guyon, I., and A. Elisseeff, 2003, An introduction to variable and feature selection: *Journal of Machine Learning Research*, **3**, 1157–1182.
- Hajmeer, M., and I. Basheer, 2002, A probabilistic neural network approach for modeling and classification of bacterial growth/no-growth data: *Journal of Microbiological Methods*, **51**, 217–226, doi: [10.1016/S0167-7012\(02\)00080-5](https://doi.org/10.1016/S0167-7012(02)00080-5).
- Hampson, D. P., J. S. Schuelke, and J. A. Quirein, 2001, Use of multiattribute transforms to predict log properties from seismic data: *Geophysics*, **66**, 220–236, doi: [10.1190/1.1444899](https://doi.org/10.1190/1.1444899).
- Haralick, R. M., K. Shanmugam, and I. Dinstein, 1973, Textural features for image classification: *IEEE Transactions on Systems, Man and Cybernetics*, **SMC-3**, 610–621, doi: [10.1109/TSMC.1973.4309314](https://doi.org/10.1109/TSMC.1973.4309314).
- Honorio, B., A. Sanchetta, E. Pereira, and A. Vidal, 2014, Independent component spectral analysis: *Interpretation*, **2**, no. 1, SA21–SA29, doi: [10.1190/INT-2013-0074.1](https://doi.org/10.1190/INT-2013-0074.1).
- Huber, P. J., 1981, *Robust statistics*: John Wiley & Sons.
- Hughes, G., 1968, On the mean accuracy of statistical pattern recognizers: *IEEE Transactions on Information Theory*, **14**, 55–63, doi: [10.1109/TIT.1968.1054102](https://doi.org/10.1109/TIT.1968.1054102).
- Jabbar, H. K., and R. Z. Khan, 2015, Methods to avoid overfitting and underfitting in supervised machine learning (comparative study): *Computer Science, Communication & Instrumentation Devices*, 163–172.
- Jones, I. F., and I. Davison, 2014, Seismic imaging in and around salt bodies: *Interpretation*, **2**, no. 4, SL1–SL20, doi: [10.1190/INT-2014-0033.1](https://doi.org/10.1190/INT-2014-0033.1).
- Joshi, A., and M. Appold, 2016, Potential of porosity waves for methane transport in the Eugene Island field of the Gulf of Mexico basin: *Marine and Petroleum Geology*, **75**, 1–13, doi: [10.1016/j.marpetgeo.2016.04.005](https://doi.org/10.1016/j.marpetgeo.2016.04.005).
- Kim, Y., R. Hardisty, and K. J. Marfurt, 2019, Attribute selection in seismic facies classification: Application to a Gulf of Mexico 3D seismic survey and the Barnett Shale: *Interpretation*, **7**, no. 3, SE281–SE297, doi: [10.1190/INT-2018-0246.1](https://doi.org/10.1190/INT-2018-0246.1).
- Kingma, D., and J. L. Ba, 2015, Adam: A method for stochastic optimization: 3rd International Conference for Learning Representations, 1–15.
- Lachiche, N., and P. Flach, 2003, Improving accuracy and cost of two-class and multi-class probabilistic classifiers using ROC curves: *Proceedings of the 20th International Conferences on Machine Learning*, 416–423.
- Li, F., and W. Lu, 2014, Coherence attribute at different spectral scales: *Interpretation*, **2**, no. 1, SA99–SA106, doi: [10.1190/INT-2013-0089.1](https://doi.org/10.1190/INT-2013-0089.1).
- Long, Z., Y. Alaudah, M. A. Qureshi, Y. Hu, Z. Wang, M. Alfarraj, G. AlRegib, A. Amin, M. Deriche, S. Al-Dharrab,

- and H. Di, 2018, A comparative study of texture attributes for characterizing subsurface structures in seismic volumes: *Interpretation*, **6**, no. 4, T1055–T1066, doi: [10.1190/INT-2017-0181.1](https://doi.org/10.1190/INT-2017-0181.1).
- Lubo-Robles, D., and K. J. Marfurt, 2019, Independent component analysis for reservoir geomorphology and unsupervised seismic facies classification in the Taranaki Basin, New Zealand: *Interpretation*, **7**, no. 3, SE19–SE42, doi: [10.1190/INT-2018-0109.1](https://doi.org/10.1190/INT-2018-0109.1).
- Masters, T., 1995, *Advanced algorithms for neural networks*: John Wiley & Sons.
- Meyer, D. E., E. L. Harvey, T. E. Bulloch, J. C. Vonnannon, and T. M. Sheffield, 2001, Use of seismic attributes in 3-D geovolume interpretation: *The Leading Edge*, **20**, 1377–1400, doi: [10.1190/1.1486768](https://doi.org/10.1190/1.1486768).
- Pearson, K., 1894, Contributions to the mathematical theory of evolution: *Philosophical Transactions A*, **185**, 71–110, doi: [10.1098/rspl.1893.0079](https://doi.org/10.1098/rspl.1893.0079).
- Posamentier, H. W., and V. Kolla, 2003, Seismic geomorphology and stratigraphy of depositional elements in deep-water settings: *Journal of Sedimentary Research*, **73**, 367–388, doi: [10.1306/111302730367](https://doi.org/10.1306/111302730367).
- Qi, J., and J. P. Castagna, 2013, Application of a PCA fault-attribute and spectral decomposition in Barnett shale fault detection: 83rd Annual International Meeting, SEG, Expanded Abstracts, 1421–1425, doi: [10.1190/segam2013-0674.1](https://doi.org/10.1190/segam2013-0674.1).
- Qi, J., T. Lin, T. Zhao, F. Li, and K. J. Marfurt, 2016, Semi-supervised multiattribute seismic facies analysis: *Interpretation*, **4**, no. 1, SB91–SB106, doi: [10.1190/INT-2015-0098.1](https://doi.org/10.1190/INT-2015-0098.1).
- Qi, J., and K. Marfurt, 2019, Nonparallelism attributes and data adaptive Kuwahara image processing: 89th Annual International Meeting, SEG, Expanded Abstracts, 1858–1861, doi: [10.1190/segam2019-3216022.1](https://doi.org/10.1190/segam2019-3216022.1).
- Qi, J., B. Zhang, B. Lyu, and K. Marfurt, 2020, Seismic attribute selection for machine-learning-based facies analysis: *Geophysics*, **85**, no. 2, O17–O35, doi: [10.1190/geo2019-0223.1](https://doi.org/10.1190/geo2019-0223.1).
- Roden, R., T. Smith, and D. Sacrey, 2015, Geologic pattern recognition from seismic attributes: Principal component analysis and self-organizing maps: *Interpretation*, **3**, no. 4, SAE59–SAE83, doi: [10.1190/INT-2015-0037.1](https://doi.org/10.1190/INT-2015-0037.1).
- Roy, A., A. S. Romero-Peláez, T. J. Kwiatkowski, and K. J. Marfurt, 2014, Generative topographic mapping for seismic facies estimation of a carbonate wash, Veracruz Basin, southern Mexico: *Interpretation*, **2**, no. 1, SA31–SA47, doi: [10.1190/INT-2013-0077.1](https://doi.org/10.1190/INT-2013-0077.1).
- Sokolova, M., N. Japkowicz, and S. Szpakowicz, 2006, Beyond accuracy, F-score and ROC: A family of discriminant measures for performance evaluation: *Australasian Joint Conference on Artificial Intelligence*, 1015–1021, doi: [10.1007/11941439_114](https://doi.org/10.1007/11941439_114).
- Sokolova, M., and G. Lapalme, 2009, A systematic analysis of performance measures for classification tasks: *Information Processing and Management*, **45**, 427–437, doi: [10.1016/j.ipm.2009.03.002](https://doi.org/10.1016/j.ipm.2009.03.002).
- Spearman, C., 1904, The proof and measurement of association between two things: *American Journal of Psychology*, **15**, 72–101, doi: [10.2307/1412159](https://doi.org/10.2307/1412159).
- Specht, D. F., 1990, Probabilistic neural networks: *Neural Networks*, **3**, 109–118, doi: [10.1016/0893-6080\(90\)90049-Q](https://doi.org/10.1016/0893-6080(90)90049-Q).
- Walden, A. T., 1985, Non-Gaussian reflectivity, entropy, and deconvolution: *Geophysics*, **50**, 2862–2888, doi: [10.1190/1.1441905](https://doi.org/10.1190/1.1441905).
- Wang, Z., C. Yin, X. Lei, F. Gu, and J. Gao, 2015, Joint rough sets and Karhunen-Loève transform approach to seismic attribute selection for porosity prediction in a Chinese sandstone reservoir: *Interpretation*, **3**, no. 4, SAE19–SAE28, doi: [10.1190/INT-2014-0268.1](https://doi.org/10.1190/INT-2014-0268.1).
- Wrona, T., I. Pan, R. L. Gawthorpe, and H. Fossen, 2018, Seismic facies analysis using machine learning: *Geophysics*, **83**, no. 5, O83–O95, doi: [10.1190/geo2017-0595.1](https://doi.org/10.1190/geo2017-0595.1).
- Wu, X., L. Liang, Y. Shi, and S. Fomel, 2019, FaultSeg3D: Using synthetic data sets to train an end-to-end convolutional neural network for 3D seismic fault segmentation: *Geophysics*, **84**, no. 3, IM35–IM45, doi: [10.1190/geo2018-0646.1](https://doi.org/10.1190/geo2018-0646.1).
- Zhao, T., V. Jayaram, A. Roy, and K. J. Marfurt, 2015, A comparison of classification techniques for seismic facies recognition: *Interpretation*, **3**, no. 4, SAE29–SAE58, doi: [10.1190/INT-2015-0044.1](https://doi.org/10.1190/INT-2015-0044.1).
- Zhao, T., F. Li, and K. J. Marfurt, 2018, Seismic attribute selection for unsupervised seismic facies analysis using user-guided data-adaptive weights: *Geophysics*, **83**, no. 2, O31–O44, doi: [10.1190/geo2017-0192.1](https://doi.org/10.1190/geo2017-0192.1).



David Lubo-Robles received a B.S. in geophysical engineering from Simon Bolivar University, Venezuela, and an M.S. in geophysics from the University of Oklahoma under K. J. Marfurt. He is a student member of SEG and is currently pursuing a Ph.D. in geophysics at the University of Oklahoma, studying under K. J. Marfurt and M.

Pranter. His research interests include the development and application of modern machine learning and pattern recognition techniques, together with quantitative interpretation skills, including prestack inversion and seismic attribute analysis to delineate geologic features amenable to hydrocarbon accumulation.



Thang Ha is a Ph.D. student in geophysics, specialized in programming and software development.



S. Lakshmivaran is currently a George Lynn Cross Research Professor Emeritus at the School of Computer Science, University of Oklahoma, Norman, OK. His research interests include data analytics, dynamic data assimilation, nonlinear dynamics, and their applications. He is a life fellow of IEEE and a fellow of ACM.



Kurt Marfurt received an M.S. and a Ph.D. in applied geophysics from Columbia University in the City of New York and an A.B. in physics and French from Hamilton College. He is a research professor of geophysics at the University of Oklahoma, where he mentors students and conducts research to aid seismic interpretation.

His experience includes 23 years as an academician, first at Columbia University, then later at the University of Houston and the University of Oklahoma. At the University of Oklahoma, he leads the AASPI consortium with the goal

of developing and calibrating new seismic attributes to aid in seismic processing, seismic interpretation, and data integration using interactive and machine-learning tools. He currently serves as the deputy editor-in-chief for 2019–2021 for *Interpretation*, as an SEG continuing education short course instructor, and as director at large for SEG.



Matthew J. Pranter received a B.S. in geology from Oklahoma State University, a B.S. in geological engineering from the Colorado School of Mines, an M.S. in geology from Baylor University, and a Ph.D. in geology from the Colorado School of Mines. He is the Victor E. Monnett Endowed Chair in energy resources and a professor of geosciences at the University of Oklahoma. He

was previously a geology professor at the University of Colorado Boulder and a senior research/reservoir geologist with ExxonMobil Upstream Research Company and Conoco. His research interests include reservoir characterization, petroleum geology, sedimentary geology, applied structural geology, and reservoir modeling.